remote sensing

MDPI

Article

SOBLE-Top5: A Stacking Ensemble Learning-Based Seasonal Downscaling Inversion Framework for Surface Soil Moisture Using Multi-Source Data

Shengmin Zhu [1], Haiyang Yu [1,*], Bingqian Ji [1], Qi Liu [1] and Deng Pan [2,3]

[1] School of Surveying and Land Information Engineering, Henan Polytechnic University, Jiaozuo 454000, China; 212304020095@home.hpu.edu.cn (S.Z.); 212304020092@home.hpu.edu.cn (B.J.); 212304020025@home.hpu.edu.cn (Q.L.)
[2] School of Water Resources and Environment, China University of Geosciences (Beijing), Beijing 100083, China; pandeng@email.cugb.edu.cn
[3] Institute of Natural Resources Monitoring and Comprehensive Land Improvement of Henan Province, Zhengzhou 450016, China
* Correspondence: yuhaiyang@hpu.edu.cn

Highlights

What are the main findings?

- A season-adaptive downscaling framework integrating the SOBLE-Top5 stacking ensemble substantially improves the SSM estimation accuracy and stability across seasons.
- A multi-scale drought analysis reveals the expansion of low-SSM areas in the study area from March to July, peaking in May–June, and highlights pronounced north–south gradients and spatial heterogeneity.

What are the implications of the main findings?

- The methodological innovation provides a reliable technical approach for high-resolution, season-adaptive SSM estimation and multi-temporal soil moisture studies.
- The multi-scale characterization of drought evolution offers robust evidence to support regional agricultural drought monitoring, water management, and resource planning.

Abstract

Surface soil moisture (SSM) serves as a critical indicator for regional water cycles, agricultural management, and drought monitoring. However, existing the SMAP data suffers from limited spatial resolution, making it challenging to meet the demands of large-scale, high-resolution applications. Taking Henan Province, located in east-central China with a continental monsoon climate and marked seasonal variability, as the study area, this research integrates multi-source data to develop a seasonal modeling strategy. Based on stacking ensemble learning, the SSM downscaling inversion model (SOBLE-Top5) is constructed. SHAP value attribution analysis is employed to reveal the primary drivers of seasonal dynamics. The results indicate: (1) The SSM exhibits distinct seasonal characteristics. Compared to the all-season modeling, the RMSE and R^2 metrics significantly improve during spring and summer. The winter ET and RF models show an approximately 9–14% higher R^2 and a 47–50% lower RMSE. (2) The SOBLE-Top5 strategy achieved up to a 4.65% higher R^2 and a 21.22% lower RMSE compared to the optimal single base model. (3) Spatial variations in the SSM characteristics reveal stable performance during the winter. The spring saw slight SSM declines in the northern regions due to rising temperatures. The study area reached its annual low (<0.08 m^3/m^3) in May–June. Driven by flood season

Check for updates

Academic Editor: Dusan Gleich

Received: 23 December 2025
Revised: 4 February 2026
Accepted: 9 February 2026
Published: 13 February 2026

Copyright: © 2026 by the authors. Licensee MDPI, Basel, Switzerland. This article is an open access article distributed under the terms and conditions of the Creative Commons Attribution (CC BY) license.

precipitation, July–August witnessed local increases exceeding 52%. The autumn exhibited a stable-then-rising trend with pronounced north–south gradient characteristics. (4) The SHAP analysis indicates that the winter SSM is primarily controlled by bulk density and clay content. The spring SSM is most influenced by LST, followed by bulk density. The summer and the autumn SSM are synergistically driven by multiple factors including elevation, temperature, and precipitation, with the summer precipitation exerting the most significant impact on instantaneous SSM variations.

Keywords: downscaling inversion; seasonal modeling; SOBLE-Top5 model; drought analysis; driving factors

1. Introduction

Surface soil moisture (SSM) represents a fundamental state variable of the Earth's surface system. It plays a dynamic regulatory role in key processes such as energy exchange at the land–atmosphere interface, hydrological responses within watersheds, ecosystem carbon cycling, and agricultural productivity. Moreover, SSM serves as both a storage reservoir for precipitation and radiative anomalies and a critical medium facilitating multi-layer interactions within the land–atmosphere system [1,2].

At present, SSM monitoring is mainly conducted through two approaches: ground stations and remote sensing satellites [3]. Traditional ground monitoring stations are limited in number and unevenly distributed [4], making them insufficient to accurately characterize large-scale soil moisture based solely on in situ observations. Microwave remote sensing provides an efficient approach for acquiring spatiotemporally continuous surface soil moisture information across large areas. However, because of the inherent physical constraints of microwave sensors, passive microwave remote sensing data are characterized by intrinsically low spatial resolution [5], which substantially limits the applicability of soil moisture products for precision crop management [6], fine-scale drought monitoring [7], ecological process simulation, high-precision water cycle assessment, and natural disaster early warning.

Satellite remote sensing, with its capability for large-scale and continuous observations, serves as the primary approach for monitoring the SSM. Active microwave sensors measure radar backscatter to achieve global, all-weather, and day–night monitoring [8], while passive microwave sensors retrieve the SSM by relating brightness and temperature to the soil dielectric constant. Over the past several decades, different microwave remote sensing techniques have been applied for SSM monitoring, including active microwave sensors such as the Advanced Scatterometer (ASCAT) [9] and the C-band Synthetic Aperture Radar (C-SAR) instrument aboard the Sentinel-1 satellite [10]. Passive microwave missions include the Advanced Microwave Scanning Radiometer for Earth Observing System (AMSR-E) [11], the Advanced Microwave Scanning Radiometer 2 (AMSR-2) [12], and the Soil Moisture and Ocean Salinity (SMOS) [13], followed by the active–passive Soil Moisture Active Passive (SMAP) mission [14], as well as China's independently developed Fengyun-3 (FY-3) [15] and HY-2 [16] satellite series. Collectively, these missions have progressively formed a multi-source satellite observation system that provides global coverage. In large-scale SSM fine-scale estimation, L-band microwave radiation has been identified as the most suitable frequency range for soil moisture retrieval because of its strong capability to penetrate vegetation canopies and its minimal atmospheric attenuation [17]. The SMAP retrieves soil moisture through the synergy of active and passive microwave observations. Although radar failure restricts its high-resolution measurements, the application of the

Backus–Gilbert (BG) interpolation method [18] effectively improves the spatial resolution. Compared with the ERA5 reanalysis data, the SMAP shows smaller systematic biases [19], underscoring its reliability for global soil moisture monitoring.

In recent years, surface soil moisture downscaling has made continuous progress in both theory and methodology. Review studies have summarized major downscaling frameworks—physically based scaling/disaggregation, active–passive or optical–microwave fusion, and statistical and machine learning approaches—and emphasized that, under highly heterogeneous land-surface conditions, scale mismatch, dependence on auxiliary variables, and limited cross-regional generalization remain the key challenges. The DISPATCH algorithm, grounded in physical and theoretical scaling principles, integrates the land surface temperature and vegetation indices to translate soil-temperature variability into soil-moisture variability, thereby improving the representation of fine-scale spatial details in coarse-resolution products [20]. However, pronounced seasonal variability and factors such as cloud contamination and dense vegetation can limit the stability of a single mapping relationship across spatiotemporal contexts [21].

Furthermore, El Hajj et al. combined X-band SAR with optical imagery through change detection to capture surface soil-moisture variations, demonstrating its utility for irrigation management and crop monitoring, though transferability across regions and land cover types warrants further validation [22]. Sun et al. coupled satellite soil moisture, in situ observations, the HYDRUS-1D model, and the Ensemble Kalman Filter (EnKF) assimilation to establish an irrigation-district-scale evaluation framework, but its scalability can be constrained by the need for comprehensive field data and site-specific parameterization [23]. Jiang et al. proposed the STC-CycleGAN model, enabling the physically consistent downscaling of global daily soil moisture from 36 km to 9 km through spatiotemporal feature constraints [24]. Xu et al. further introduced a CNN-based downscaling method with an input weighting layer to predict the residual soil moisture, achieving an enhanced estimation accuracy [25]. Nevertheless, kilometer-scale products (e.g., 9 km) may still be insufficient for local applications over large heterogeneous regions, and the model robustness remains sensitive to training sample distributions and seasonal backgrounds.

The successful application of machine learning (ML) in ecology, soil science, and meteorology has driven the rapid development of data-driven soil moisture downscaling approaches. For example, using South Korea and Australia as study areas, the AMSR-E soil moisture was downscaled with single-model approaches such as RF, BRT, and Cubist to enhance the spatial resolution; however, the validation results did not adequately represent mid-elevation regions [26]. Wang et al. combined RF, LightGBM, XGBoost, and DSCGAN within a super-resolution framework in the Lightning River Basin, leveraging high-resolution information such as the MODIS vegetation indices and LST to enrich the spatial details of coarse-resolution microwave soil moisture [27]. Jeran Poehls employed several lightweight models (Dense, Prob, WDL, and RF) to downscale the soil moisture to a sub-kilometer resolution, highlighting the feasibility of obtaining higher-spatial-resolution products at relatively low computational cost, but he reported that the models were unreliable over cropland areas [28]. Meanwhile, Koujani applied an RF-based downscaling approach incorporating multi-source geographic features across six agricultural regions to downscale the GLDAS soil moisture; the correlation and R^2 in humid regions reached 0.74 and 0.85, respectively, whereas the correlation decreased in semi-humid and arid regions [29]. Collectively, these studies demonstrate that ML can effectively exploit multi-source predictors to improve the downscaling performance. Nevertheless, two common characteristics emerge: many studies conduct the validation using specific test sites, crop/irrigation conditions, or data settings, with limited evidence of generalization to broader spatial domains; and the existing work often emphasizes the comparison and selec-

tion of a single simple "best" model, with a limited adaptation of training. Simultaneously, multiple studies have shown that in large-area regions with highly heterogeneous surface conditions or complex topography, downscaling the SMAP or the ESA CCI soil moisture products from coarse resolutions of approximately 25–36 km to 1–5 km typically results in correlation coefficients ranging from 0.5 to 0.7 and RMSE values of about 0.04–0.06 m^3/m^3 when compared with in situ observations [30,31]. Although spatial resolution is improved to some extent, such accuracy levels and spatial scales still exhibit clear limitations for fine-scale applications.

Based on the above research status, SSM downscaling still faces the following challenges: (1) the current methods often lack sufficient accuracy and spatial resolution for large, heterogeneous regions; (2) the pronounced seasonal variability in temperate continental monsoon climates reduces the effectiveness of uniform training strategies; and (3) most studies focus on single-model comparisons, neglecting model transferability and the potential of ensemble approaches for error mitigation. These limitations constrain the reliability and generalizability of a downscaled SSM under complex geological, hydrological, and climatic conditions.

To address the above challenges, this study focuses on the following aspects: (1) integrating the SMAP soil moisture data with multi-source auxiliary variables—including spectral, meteorological, hydrological, topographical, and soil texture factors—to establish a multi-source driven downscaling inversion framework, thereby enhancing the spatial representation of the surface soil moisture; (2) introducing a seasonal modeling strategy to optimize the model training with daily-scale datasets, enabling a more accurate characterization of the seasonal climatic variability and improving the precision of the SMAP soil moisture downscaling; and (3) employing an ensemble learning framework to fuse the predictions from multiple models, thereby exploiting the inter-model error compensation to enhance the accuracy, robustness, and generalization capability of the downscaling results.

2. Materials and Methods

2.1. Overview of the Study Area

Henan Province (31°23′–36°22′N, 110°21′–116°39′E), located in the southern North China Plain and covering 167,000 km^2, represents a typical agricultural region. The terrain descends from the Taihang and Funiu Mountains in the west to the Huang–Huai–Hai alluvial plain in the east, forming a diverse landscape of mountains, hills, basins, and plains. The province experiences a transitional monsoon climate between warm temperate and northern subtropical zones, featuring four distinct seasons, mean annual temperatures of 12–16 °C, and precipitation of 500–900 mm, synchronized with the thermal regime. Over 60% of the land is cultivated, mainly for wheat and maize. The interplay of complex topography and intensive agriculture induces strong spatiotemporal variability in soil moisture, making Henan an ideal region for investigating seasonal dynamics and spatial heterogeneity in SSM downscaling (Figure 1). Specifically, this study covers the period from December 2023 to November 2024.

2.2. Data Acquisition and Preprocessing

Based on commonly used SSM remote sensing influence factors and relevant meteorological [31], hydrological [32], vegetation index [33], and ancillary variables [34] identified in previous studies, the required datasets were acquired from Google Earth Engine and the corresponding official data repositories (Table 1). Low-resolution soil moisture products, remote sensing imagery, and auxiliary datasets were subjected to a series of preprocessing steps, including band extraction, spatial resampling, and clipping to the study area. All

datasets were then standardized to the WGS84 geographic coordinate system to ensure spatial consistency.

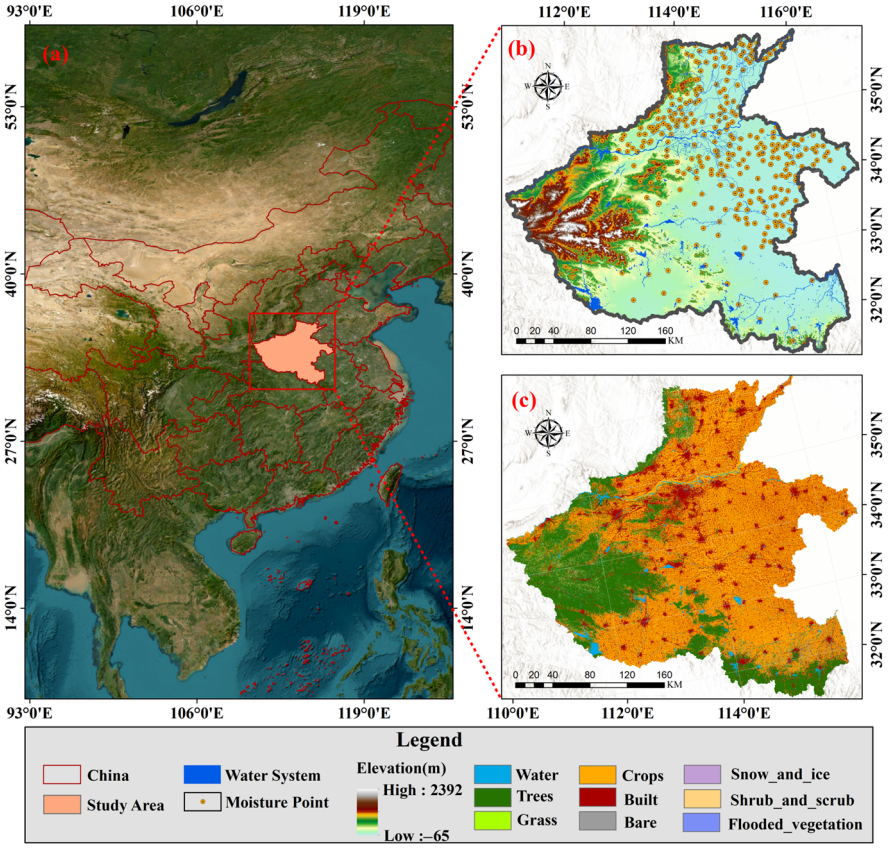


Figure 1. Schematic map of study area distribution. (**a**) Geographic location of the study area; (**b**) Elevation distribution and spatial distribution of moisture points; (**c**) Spatial distribution of land cover types.

Table 1. Description of datasets used in this study.

Category	Source of the Dataset	Variable	Spatial Resolution	Temporal Resolution
Soil moisture data	NASA/SMAP/SPL4SMGP/008 *	SSM	9 km	3 h
Remotely sensed data	MODIS/061/MCD43A3 *	WHR-VIS WHR-NIR	500 m	Daily
	MODIS/061/MOD09GA *	NDVI NMDI NDWI EVI	500 m	Daily
	MODIS/061/MCD15A3H *	LAI	500 m	4-day
	GOOGLE/DYNAMICWORLD/V1 *	Land cover (LC)	10 m	-
Meteorological data	MODIS/061/MOD11A1 *	LST	1 km	Daily
	UCSB-CHG/CHIRPS/DAILY *	Precipitation	0.05°	Daily
Auxiliary data	HWSD (FAO Soils Portal)	Sand Silt Clay Bulk density (BD)	1 km	-
	NASADEM_HGT v001 *	Slope Aspect Elevation	30 m	-
	USGS/SRTMGL1_003 *	Wetness index (TWI)	30 m	-
In situ site data	-	Soil moisture (10 cm)	-	Daily

Datasets with * were accessed via Google Earth Engine (GEE). For datasets not available in GEE, the official provider/source is reported (e.g., HWSD v2.0 was obtained from the FAO Soils Portal).

2.2.1. SMAP L4 SSM Product

The NASA SMAP mission, launched on 31 January 2015, was designed to acquire global soil moisture and freeze–thaw status via L-band active and passive microwave observations. Following a radar failure in July 2015, high-resolution (3 km) products became unavailable. This study employed the SMAP L4 3-hourly 9-km surface and root-zone soil moisture dataset (abbreviated as SMAP L4 SSM), which was temporally aggregated to generate the continuous daily soil moisture time series.

2.2.2. Remotely Sensed Data

The Moderate Resolution Imaging Spectroradiometer (MODIS) represents a primary data source for constructing downscaling predictors, offering continuous observations of key parameters such as spectral indices and land surface temperature at spatial resolutions of 500 m to 1 km. For this study, the MOD09GA, MCD43A3, and MCD15A3H products were selected, and daily observations corresponding to the study period were obtained via the Google Earth Engine platform.

MOD09GA V6.1 products, acquired from the MODIS sensor onboard NASA's Terra satellite, provide atmospherically corrected surface reflectance data across seven spectral bands at 500 m spatial resolution. To mitigate the effects of cloud contamination and atmospheric interference, high-quality pixels were selected based on quality control (QC) information. Missing pixels were subsequently filled using temporal interpolation. Vegetation indices were then derived using the following formula:

$$NDVI = \frac{\rho_{nir} - \rho_{red}}{\rho_{nir} + \rho_{red}} \quad (1)$$

$$EVI = G \times \frac{\rho_{nir} - \rho_{red}}{L + \rho_{nir} + C_1 \times \rho_{red} - C_2 \times \rho_{blue}} \quad (2)$$

$$NDWI = \frac{\rho_{nir} - \rho_{swir1}}{\rho_{nir} + \rho_{swir1}} \quad (3)$$

$$NMDI = \frac{\rho_{swir2} - (\rho_{nir} + \rho_{swir3})}{\rho_{swir2} + (\rho_{nir} + \rho_{swir3})} \quad (4)$$

Here, ρ_{nir}, ρ_{red}, and ρ_{blue} denote the reflectance in the near-infrared, red, and blue bands, respectively. ρ_{swir1}, ρ_{swir2}, ρ_{swir3} represent the reflectance in the shortwave infrared bands 1, 2, and 3, respectively. G = 2.5 is the gain coefficient, the canopy background adjustment coefficient L = 1, and C1 = 6.0 and C2 = 7.5 are aerosol resistance weights [35].

MCD43A3 V6.1 products, with a native spatial resolution of 500 m, derived from 16-day sliding window observations, provide daily black-sky (BHR) and white-sky albedo (WHR) via BRDF modeling [36]. Unlike BHR, WHR is independent of solar zenith angle, making it more suitable for cloudy or diffuse light conditions. In this study, WHR in the visible (WHR-VIS) and near-infrared (WHR-NIR) bands were used as downscaling predictors.

MCD15A3H is a global Leaf Area Index (LAI) and Fraction of Photosynthetically Active Radiation (FPAR) product provided by MODIS with a spatial resolution of 500 m and a temporal resolution of 4 days. The product is derived from observations by the Terra and Aqua satellites using radiative transfer model inversion. Since LAI products are highly susceptible to cloud contamination, we first performed strict pixel-level screening to remove low-quality observations. We then reconstructed the missing values generated after QC screening using temporal interpolation, thereby obtaining a spatially complete and temporally continuous daily LAI time series for subsequent analysis.

Dynamic World V1 is a near real-time global 10 m resolution land use/land cover (LULC) product derived from Sentinel-2 imagery by Google and WRI. Using deep learning

based automated classification, it provides pixel-level probabilities for nine land cover classes: cropland, trees, shrubs, grassland, wetlands, buildings, structures, standing water, and ice/snow. In this study, Dynamic World V1 served as a land cover predictor for soil moisture downscaling.

2.2.3. Meteorological Data

Land surface temperature (LST) is a critical variable for SSM estimation [37]. The MOD11A1 V6.1 product from the Terra sensor provides daily 1 km LST data using the Split-Window algorithm, accounting for atmospheric effects such as water vapor and cloud cover [38]. Daytime LST was used to match this study's temporal scale. To mitigate cloud contamination and noise, high-quality pixels (QC = 0) were retained, and temporal interpolation was applied to fill gaps and smooth short-term fluctuations. In addition, spatial Gaussian filtering (10 × 10 pixels, σ = 1) was used to smooth anomalies and fill local gaps. The processed daily LST images were then clipped to the study area.

Precipitation is a key factor controlling soil moisture dynamics. This study employed the CHIRPS v2.0 dataset, which integrates 0.05° satellite observations with in situ station measurements and atmospheric model outputs, providing global precipitation data from 1981 to present for downscaling analysis. In practice, same-day (daily) precipitation coincident with SMAP overpass dates was used as the baseline precipitation predictor in the downscaling framework. To explicitly evaluate the potential contribution of antecedent precipitation (i.e., memory effects), we further conducted a sensitivity analysis by constructing two enhanced precipitation predictors, P14 and API090 (their mathematical definitions and parameter settings are provided in Appendix A.3).

2.2.4. Ancillary Data

Soil property data serve as key predictors influencing soil moisture estimation, as soil permeability and water-holding capacity directly regulate the dynamic processes of SSM. In this study, soil property data were obtained from the Harmonized World Soil Database (HWSD v2.0). Constructed based on the FAO-90 soil classification system, this dataset provides morphological, chemical, and physical soil attributes at an approximate spatial resolution of 1 km, encompassing both topsoil and subsoil layers. Specifically, the clay, sand, and silt fractions, along with bulk density (BD) from the topsoil layer, were extracted and clipped to the boundaries of the study area.

Topographic factors, strongly linked to climate, runoff, and hydrological processes, significantly influence the spatial distribution of surface soil moisture. Previous studies have shown that terrain parameters, especially elevation and slope, are valuable for SSM downscaling [39]. In this study, topographic data were obtained from the NASA Digital Elevation Model (NASADEM), which refines the Shuttle Radar Topography Mission (SRTM) using auxiliary datasets including ICESat, ASTER GDEM, and Landsat imagery. Compared with SRTM, NASADEM provides higher accuracy through gap filling and error correction, along with derivative layers such as slope, aspect, and surface roughness. Elevation, slope, and aspect at 30 m resolution were used in this analysis.

Additionally, the Terrain Wetness Index (TWI) was computed to characterize the topographic control on surface soil moisture. The TWI was derived using the Shuttle Radar Topography Mission (SRTM) data in conjunction with Hydro SHEDS runoff area information, following the formulation proposed by Beven and Kirkby [40]:

$$Slope(radian) = tan\left(\frac{slope(deree) \times \pi}{180}\right) \quad (5)$$

$$TWI = ln\left(\frac{flow\ accumultion}{tan(slope)}\right) \quad (6)$$

Among these parameters, slope values were derived from the SRTM DEM and converted to radians to improve computational precision, while flow accumulation areas were obtained from the Hydro SHEDS 15-arcsecond flow accumulation dataset.

2.2.5. In Situ Site Data

Ground-based SSM observations were provided by the Jiaozuo Hydrological Bureau, encompassing 322 monitoring stations. Each station recorded measurements six times daily (0:00, 4:00, 8:00, 12:00, 16:00, and 20:00) at three standard soil depths—10 cm, 20 cm, and 40 cm. Focusing on daily surface soil moisture dynamics, only the 10 cm observations were used in this study. Prior to daily aggregation, the in situ measurements underwent quality control to ensure data reliability. Specifically, observations falling outside the physically plausible range were first removed, followed by statistical outlier detection to eliminate anomalous values deviating markedly from the station-specific distribution. The remaining valid measurements were then averaged to derive daily SSM values for subsequent analysis. The SMAP L4 product represents soil moisture at a 5 cm depth, whereas the ground-truth data used for downscaling validation were collected at 10 cm. Although this depth difference may introduce minor uncertainty, soil moisture across adjacent layers typically exhibits a strong correlation [41].

2.3. Research Methods

2.3.1. Downscaling Framework

During the data processing stage, different types of remote sensing, meteorological, soil property, and auxiliary datasets were subjected to targeted, type-specific processing, including quality control, Gaussian filtering, gap filling, factor calculation, and band extraction, thereby generating the predictors used for downscaling. To ensure spatial-scale consistency between predictors and the SMAP target, all predictor variables were first resampled to the SMAP grid resolution (9 km). These 9 km downscaling factors were paired with SMAP L4 SSM at 9 km to construct the modeling samples. A seasonal modeling strategy was adopted. For each season, the 9 km samples were split into training and testing subsets (70%/30%). The SMAP SSM at 9 km was used as the target variable. Multiple base learners were trained using the 9 km resampled from the training set, and their performance was evaluated through five-fold cross-validation. The top 2–5 base learners were selected according to their mean cross-validated and further tuned, after which an ensemble model was constructed and validated on the held-out 9 km testing subset. After model training and validation at 9 km, 1 km predictor images were introduced only in the inference stage. Specifically, the trained seasonal ensemble model was applied to the wall-to-wall 1 km predictor grids over the study area to generate the final downscaled SSM maps at 1 km resolution. The overall workflow is summarized in Figure 2.

2.3.2. Model Description

1. Deep Neural Networks

Deep neural networks [42], as the core architecture of deep learning, achieve efficient modeling of complex nonlinear relationships by simulating the hierarchical information processing of biological neural systems.

$$h^{(l)} = \sigma\left(W^{(l)}h^{(l-1)} + b^{(l)}\right),\ \ l = 1, \ldots, L \quad (7)$$

where $h^{(0)} = x$ denotes the input feature, $\sigma(.)$ is the nonlinear activation function, and $W^{(l)}$ and $b^{(l)}$ represent the parameters of the layer. The model comprises three hidden layers (128-64-32) that automatically extract multi-level abstract features via fully connected structures and nonlinear activations. Training employs the Adam optimizer with regularization, incorporating early stopping and cross-validation to enhance robustness.

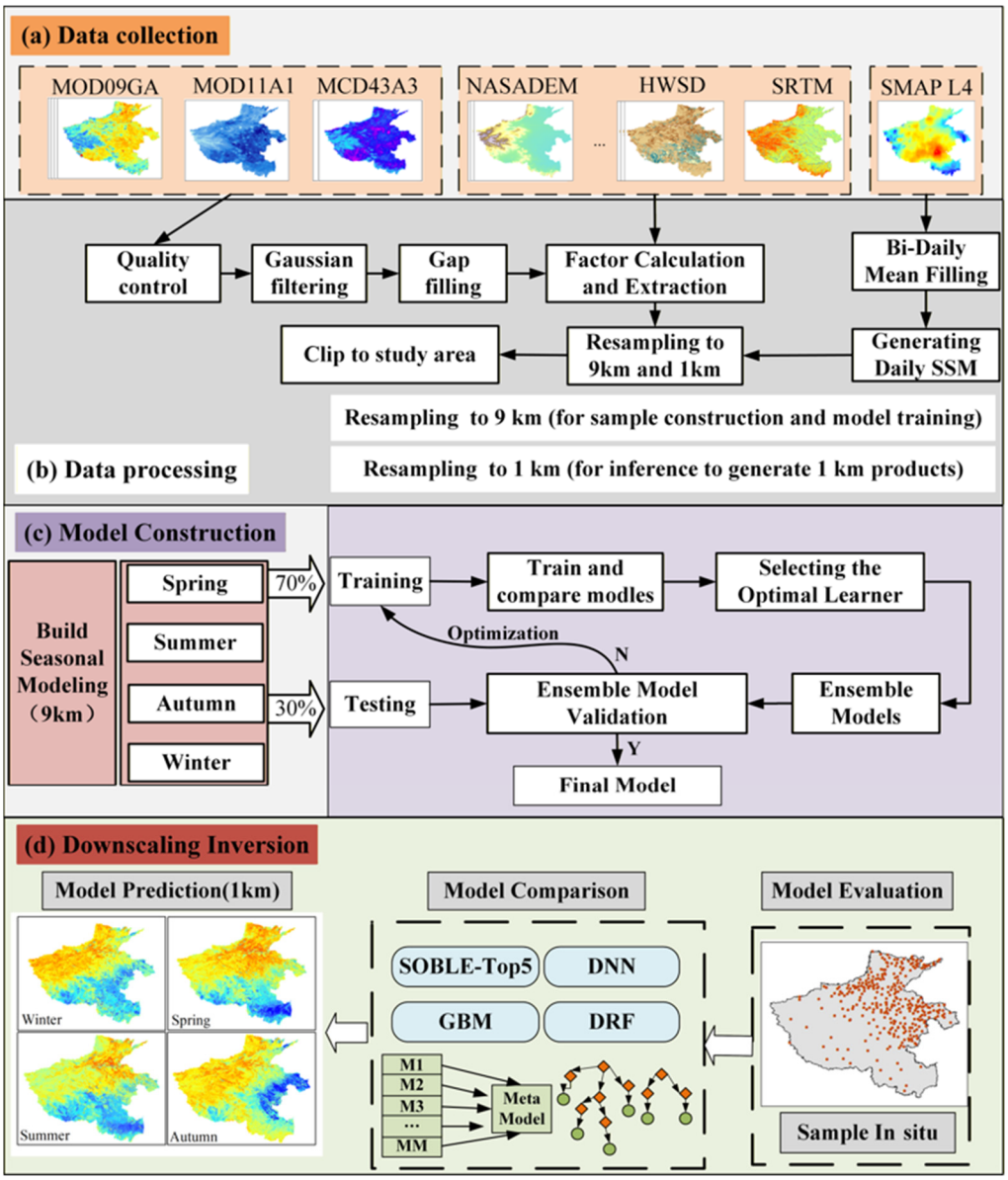


Figure 2. Workflow of the ensemble learning framework for generating 1 km resolution for SSM products.

2. Gradient Boosting Machine

Gradient Boosting Machine [43] is an advanced algorithm based on the Boosting ensemble learning framework. Its core idea involves progressively optimizing the loss function:

$$F_m(x) = F_{m-1}(x) + \gamma_m h_m(x) \quad (8)$$

where $h_m(x)$ is the decision tree for the m round of training and γ_m is the optimal step size. The model fits the negative gradient of the previous loss to approximate residuals, with the final prediction computed as the weighted sum of all base learners:

$$\hat{y}(x) = \sum_{m=1}^{M} \gamma_m h_m(x) \quad (9)$$

GBM model was configured with 100 trees, a maximum depth of 10, and a learning rate of 0.1. Model robustness was evaluated via five-fold cross-validation, effectively mitigating overfitting when handling high-dimensional, heterogeneous datasets such as remote sensing-derived agricultural features [44].

3. Distributed Random Forest

The Distributed Random Forest algorithm is an optimized Random Forest implementation for supervised classification and regression [45]. DRF builds multiple decision trees using dual randomness—row-wise bootstrap sampling and column-wise random feature selection—with the final prediction obtained by averaging all trees:

$$\hat{y}(x) = \frac{1}{T}\sum_{t=1}^{T} h_t(x) \quad (10)$$

where T denotes the number of trees and $h_t(x)$ represents the prediction function for the t-th tree.

4. Basic learner for Ensemble learning

Ensemble learning integrates multiple base learners to enhance model accuracy and generalization. Base learners can be homogeneous or heterogeneous: the former introduces diversity through variations in samples or features, while the latter combines algorithms with complementary mechanisms. In this study, six representative learners—Random Forest (RF), Extra Trees (ET), Categorical Boosting (CatBoost), Extreme Gradient Boosting (XGBoost), K-Nearest Neighbors (KNN), and Light Gradient Boosting Machine (LightGBM)—were automatically selected for training. These models complement each other in reducing bias and variance and differ in their handling of high-dimensional and heterogeneous remote sensing data, providing a solid foundation for ensemble modeling and performance evaluation.

2.3.3. Stacking Ensemble Method

Ensemble learning is a machine learning paradigm designed to enhance model generalization by integrating multiple base learners with diverse or complementary characteristics [46]. Stacking represents a typical model fusion approach that combines predictions from multiple base models through the training of a meta-learner, thereby exploiting inter-model complementarities to achieve improved predictive performance. The overall workflow of the stacking ensemble framework is shown in Figure 3.

1. The model training and ensemble learning workflow was implemented using the PyCaret platform. The original dataset was randomly split into fixed training (70%) and testing (30%) subsets. To ensure consistent feature scaling across input variables with different physical units, all input features were z-score standardized using training-set statistics prior to model training, and the same transformation was consistently applied during cross-validation and testing to prevent information leakage and ensure balanced model training.
2. During the training process, M base models were trained and evaluated using a five-fold cross-validation strategy to obtain out-of-fold (OOF) predictions. These OOF predictions from all folds were concatenated to construct a new feature set,

denoted as FM, which served as input for the subsequent meta-learning stage.

$$FM(x_i) = \left[\hat{y}_{j,1}^{OOF}, \hat{y}_{j,2}^{OOF}, \ldots\ldots, \hat{y}_{j,M}^{OOF}\right] \quad (11)$$

where $\hat{y}_{j,m}^{OOF}$ denotes the out-of-fold prediction for sample x_i produced by the m-th base learner (m = 1, . . ., M), which is trained on the corresponding training folds that exclude x_i.

3. The meta-learner M0 is trained on FM and the corresponding target labels to fuse the predictions from all base learners. During testing, each base learner is retrained on the full training set (70%) and used to generate predictions for the test set (30%), forming Test1, Test2, . . ., TestM. The trained M_0 then takes Test1, . . ., TestM as input to produce the final predictions.
4. The meta-learner was selected under a seasonal modeling strategy based on the mean cross-validation performance within the training set: ET was optimal for winter/summer/autumn, while RF was optimal for spring. In the stacking ensemble stage, the meta-learner takes the out-of-fold (OOF) predictions generated by the base learners under five-fold cross-validation as inputs. Since these OOF predictions correspond to the same target variable (SSM) and thus share consistent units and comparable magnitudes, and because the meta-learner is tree-based (ET/RF) and generally insensitive to linear feature scaling, no additional normalization or standardization was applied to the OOF predictions at this stage.

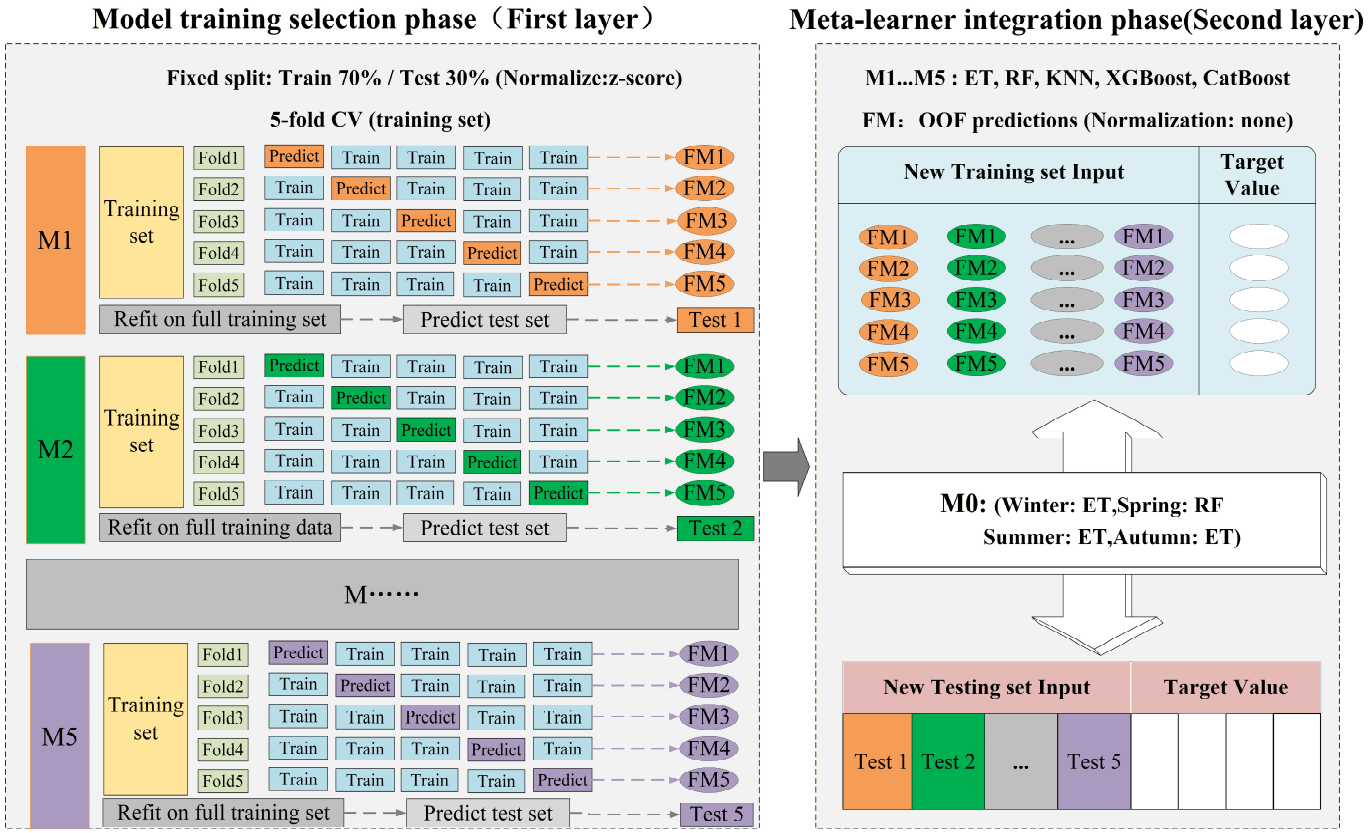


Figure 3. Schematic of the stacking ensemble framework.

Regarding the meta-learner configuration, these hyperparameter settings follow the recommended default configuration of the PyCaret AutoML framework, which is designed to balance ensemble stability, generalization performance, and computational efficiency in stacking-based learning. Specifically, both ET and RF were configured with

n_estimators = 100, max_features = 1, random_state = 123, and n_jobs = −1; ET used bootstrap = False, whereas RF used bootstrap = True. All other hyperparameters (e.g., max_depth, max_leaf_nodes, max_samples) were kept at their default values (None).

2.3.4. Seasonal Modeling Strategy

The study area exhibits distinct seasonal variability, with key drivers of soil moisture differing markedly among seasons. To evaluate the influence of seasonal dynamics on model performance, seasonal modeling was conducted based on meteorological definitions (winter: December–February, spring: March–May, summer: June–August, autumn: September–November) and compared with all-season modeling. This classification follows commonly accepted climatological conventions and does not rely on temperature-based thresholds, ensuring consistency with SMAP observation periods and facilitating cross-seasonal comparisons. Based on the seasonal partitioning described above, the samples were further split into training and testing sets at a ratio of 7:3, and the sample size for each season was summarized, as reported in Table 2.

Table 2. Seasonal sample sizes for training and testing.

Seasonal Division	Days	Training Samples	Testing Samples
Winter (December–February)	91	158,613	67,977
Spring (March–May)	92	160,356	68,724
Summer (June–August)	92	160,356	68,724
Autumn (September–November)	91	158,613	67,977
All Seasons	366	637,938	273,402

2.4. Validation Metrics

To comprehensively evaluate the performance of the proposed SSM inversion framework, five statistical metrics are employed to assess the accuracy of ensemble model soil moisture estimates. The Pearson correlation coefficient (R) and the coefficient of determination (R^2) quantify the degree of linear agreement and the proportion of variance explained between predicted and measured soil moisture, respectively. Bias is used to assess systematic overestimation or underestimation. RMSE reflects the overall magnitude of prediction errors with greater sensitivity to large deviations, whereas MAE provides a more robust measure of the average absolute error. Together, these metrics offer a comprehensive assessment of model accuracy, consistency, and reliability [47]. The aforementioned evaluation metrics were employed to assess the robustness and adaptability of the model. The corresponding statistical formulations are expressed as follows:

$$R = \frac{\sum_{i=1}^{N}\left(x_i^P - x_{Mean}^P\right)\left(x_i^M - x_{Mean}^M\right)}{\sqrt{\sum_i^N\left(x_i^P - x_{Mean}^P\right)^2}\sqrt{\sum_i^N\left(x_i^M - x_{Mean}^M\right)^2}} \tag{12}$$

$$R^2 = 1 - \frac{\sum_{i=1}^{N}\left(x_i^M - x_i^P\right)^2}{\sum_i^N\left(x_i^M - x_{Mean}^M\right)^2} \tag{13}$$

$$Bias = \frac{1}{N}\sum_i^N\left(x_i^P - x_i^M\right) \tag{14}$$

$$RMSE = \sqrt{\frac{1}{N}\sum_i^N\left(x_i^P - x_i^M\right)^2} \tag{15}$$

$$MAE = \frac{1}{N}\sum_i^N\left|x_i^P - x_i^M\right| \tag{16}$$

In the equation, N denotes the number of measured or estimated SSM sample points. Furthermore, x_i^P and x_i^M represent the i-th predicted SSM and the i-th measured SSM, respectively. x_{Mean}^P and x_{Mean}^M denote the mean values of the predicted SSM and the measured SSM, respectively. The R lies within the interval $[-1, 1]$. When R is within the interval $[0, 1]$, it indicates a positive correlation between x_i^P and x_i^M; when R is within the interval $[-1, 0]$, it indicates a negative correlation; and when R is 0, there is no correlation between the two.

3. Results

3.1. Comparative Performance of Seasonal Modeling

As summarized in Table A1 in Appendix B, the season-wise modeling strategy consistently outperformed the all-season configuration across most of the seasons. The most pronounced improvement is observed in the winter: the ET and the RF models achieve R^2 values of 0.9493 and 0.9479, respectively, representing increases of approximately 9.2% and 13.7% compared with their all-season counterparts (ET: R^2 = 0.8697; RF: R^2 = 0.8334). Correspondingly, the RMSE is reduced from 0.0299/0.0317 in the all-season models to 0.0157/0.0159, indicating decreases of about 47.5% and 49.8%, respectively, which demonstrates the clear advantage of seasonal modeling in the winter. In the spring, the RF model reduces the RMSE by 12.3% relative to the all-season RF and increases the R^2 by approximately 6.9% (0.8909 vs. 0.8334). In the summer, the ET model attains an R^2 of 0.8727, slightly higher than that of the all-season ET (R^2 = 0.8697). In the autumn, the seasonal ET model shows superior error performance, with the RMSE decreasing from 0.0299 in the all-season ET to 0.0256; although the R^2 is marginally lower (0.8647 vs. 0.8697), the overall performance remains stable. The results indicate that the performance gains of the seasonal modeling strategy do not stem from additional parameter tuning or increased model complexity; rather, they arise from explicitly accounting for season-dependent land-surface processes. Meanwhile, the strategy maintains stable performance under varying climatic conditions, providing a more physically consistent framework for the SSM estimation.

As illustrated in Figure 4 and summarized in Table A1, the all-season model consistently underperformed compared to the seasonal models in terms of both the RMSE and the R^2. A unified annual model tends to smooth or obscure season-dependent relationships, whereas season-specific training better captures the changing coupling between soil moisture and environmental drivers, resulting in an improved predictive skill. Regarding the base-learner selection, LightGBM exhibited a persistently inferior performance across all of the seasons, characterized by a higher RMSE and a lower R^2. This systematic underperformance likely reflects the sensitivity of the leaf-wise boosting to the hyperparameters governing the model complexity and regularization, which can lead to under/overfitting under heterogeneous seasonal conditions when using the default settings. Given its limited predictive contribution and the risk of injecting low-quality meta-features into the ensemble, LightGBM was excluded from the stacking ensemble. The remaining learners (ET, RF, KNN, XGBoost, and CatBoost) were retained to enhance accuracy, robustness, and generalization.

3.2. Performance of Stacking Ensemble Learning

Using the seasonal modeling strategies, the top 2–5 basic learners with the optimal R^2 values were selected for the ensemble training. Blender and stacking ensemble strategies were employed. The Blender ensemble employed a linear combination for the fusion, while the stacking ensemble utilized both a linear combination and the basic learner with the best performance prior to the ensemble training. The 5-fold cross-validation (CV) average results post-ensemble are shown in Table 3.

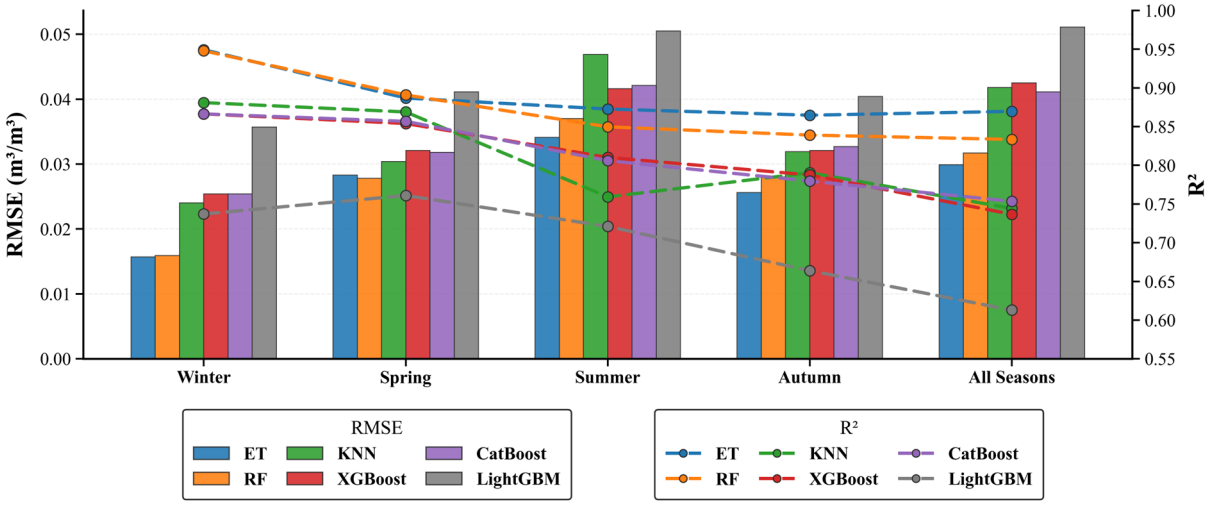


Figure 4. Comparison of model performance (RMSE and R^2) across seasons and all-season modeling.

Table 3. Comparison of model accuracy after different ensemble learning methods.

Model		Number of Ensembles	Seasonal							
			Winter		Spring		Summer		Autumn	
			RMSE	R^2	RMSE	R^2	RMSE	R^2	RMSE	R^2
Ensemble method	Blender	Top 2	0.0208	0.9127	0.0269	0.8973	0.0376	0.8449	0.0262	0.0208
		Top 3	0.0208	0.9173	0.0273	0.8942	0.0365	0.8539	0.0256	0.0208
		Top 4	0.0219	0.9078	0.0297	0.8753	0.0369	0.851	0.0259	0.0219
		Top 5	0.0232	0.8966	0.0285	0.8852	0.0366	0.853	0.0266	0.0232
	Stacking (Linear regression)	Top 2	0.019	0.9309	0.0259	0.9051	0.0329	0.8811	0.0252	0.019
		Top 3	0.0185	0.9345	0.0257	0.9064	0.0327	0.883	0.027	0.0185
		Top 4	0.0185	0.9345	0.0254	0.9087	0.0327	0.8831	0.026	0.0185
		Top 5	0.0185	0.9345	0.0247	0.87	0.0324	0.8848	0.026	0.0185
	Stacking (Optimal basic learner)	Top 2	0.0143	0.9577	0.0246	0.9141	0.0317	0.89	0.0245	0.0143
		Top 3	0.0142	0.9585	0.0221	0.9307	0.0311	0.895	0.0234	0.0142
		Top 4	0.0142	0.9585	0.0219	0.9323	0.0308	0.8963	0.0232	0.0142
		Top 5	0.0141	0.9586	0.0219	0.9323	0.0303	0.8994	0.0232	0.0141

The unit of RMSE is m^3/m^3.

The Stacking Optimal Basic Learner Ensemble Top 5 (SOBLE-Top5) strategy, which optimally combines the five base learners with the lowest RMSE, achieved the best overall performance on the seasonally segmented dataset. Compared with the top single base learner prior to the ensemble, SOBLE-Top5 increased the R^2 by 4.65%, 3.06%, 2.85%, and 0.98% in the spring, summer, autumn, and winter, respectively, while reducing the RMSE by 21.22%, 11.14%, 9.30%, and 9.55%. The stacking with linear regression approach ranked second, improving the R^2 by 1.20% and 1.39% and reducing the RMSE by 11.15% and 4.98% in the spring and summer, respectively, but showing a decreased performance in the autumn and winter, with the R^2 declining by 0.66% and 1.55% and the RMSE increasing by 1.56% and 17.83%, indicating a limited seasonal generalization. By contrast, the Blender ensemble consistently underperformed, with aggregated results below those of the best single base learner. Overall, SOBLE-Top5 demonstrated a superior predictive accuracy and robustness across all of the seasons, making it the most suitable strategy for seasonal modeling.

3.3. Multi-Model Performance Comparison and Validation

To further validate the superiority of the SOBLE-Top5 model, Table A2 compares its performance with that of the DNN, GBM, and DRF models across the training and testing phases, using the R^2, RMSE, and MAE as the evaluation metrics. SOBLE-Top5 consistently

achieved the highest accuracy in all of the seasons, with a training R^2 of 0.9323–0.9586, an RMSE of 0.0142–0.0303 m^3/m^3, and an MAE of 0.0104–0.0227 m^3/m^3, demonstrating an excellent fitting precision. In testing, it maintained superior generalization (R^2 = 0.8977–0.9632; RMSE = 0.0133–0.0291 m^3/m^3; MAE = 0.0097–0.0217 m^3/m^3). The DRF and the GBM showed a moderate performance, particularly in the winter, while the DNN exhibited the weakest adaptability (R^2 = 0.7290–0.8556; RMSE = 0.0264–0.0498 m^3/m^3; MAE = 0.0200–0.0388 m^3/m^3), reflecting a limited sensitivity to seasonal variations.

As shown in Table A2 and Figure 5, SOBLE-Top5 consistently outperformed the DNN, the GBM, and the DRF across all of the seasons. In testing, it improved the R^2 over the DNN by 11.96–24.53% while reducing the RMSE by 36.39−49.62% and the MAE by 40.00–51.50%, with the largest R^2 gain in the summer and the greatest RMSE and MAE reductions in the winter. The winter achieved the highest overall accuracy (R^2: 12.58%; RMSE: −49.62%; MAE: −51.50%), while the largest absolute error reduction occurred in the summer (RMSE: −0.0207 m^3/m^3; MAE: −0.0171 m^3/m^3). Compared with the GBM and the DRF during the optimal season, SOBLE-Top5 improved the R^2 by 5.48–5.58%, the RMSE by 35.12–35.44%, and the MAE by 37.82–38.22%, demonstrating its superior performance over both of the models.

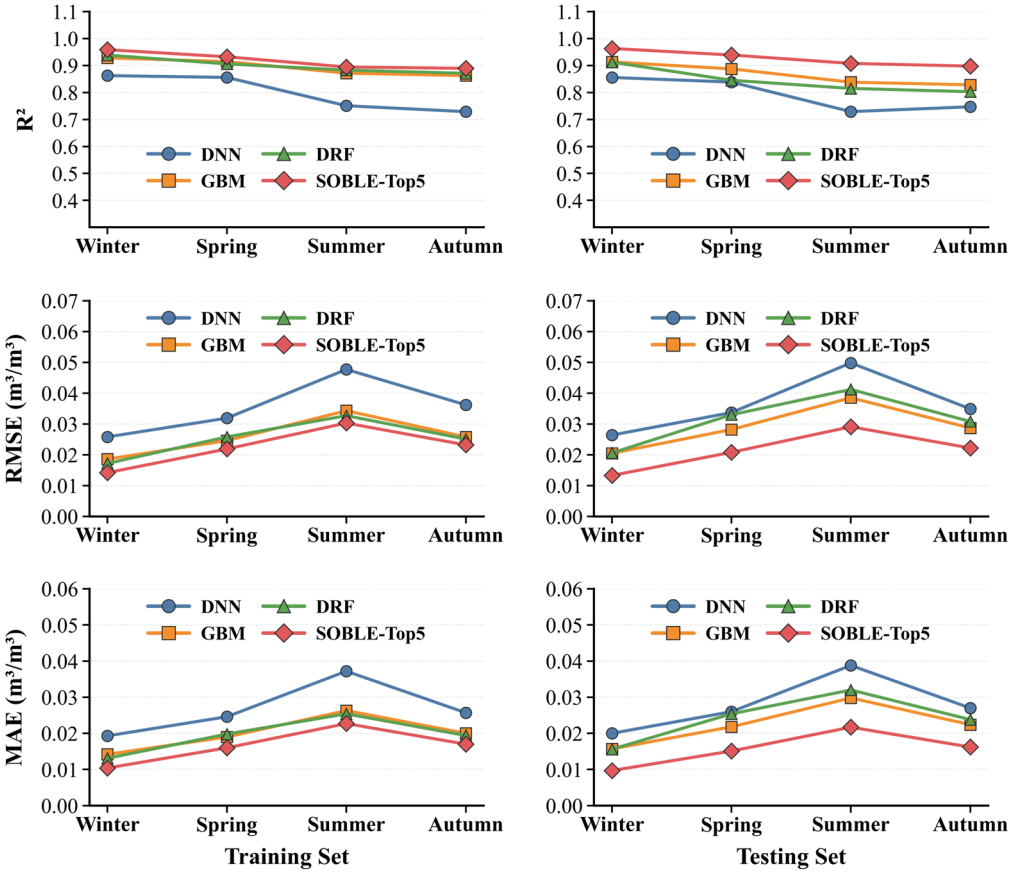


Figure 5. Seasonal performance comparison of DNN, GBM, DRF, and SOBLE-Top5 on the training and test datasets. The left column shows season-wise metrics on the training set, and the right column shows the corresponding metrics on the held-out test set; the top, middle, and bottom rows report R^2, RMSE, and MAE, respectively.

As shown in Table A2 and Figure 6, SOBLE-Top5 exhibits strong and stable predictive performance across all of the seasons (mean test set $R^2 \approx 0.93$), indicating that the ensemble maintains a good fit and generalization under the different seasonal hydro-climatic conditions. The winter exhibits relatively strong performance ($R^2 = 0.9632$; RMSE = 0.0133; MAE = 0.0097), suggesting a stronger consistency with the SMAP L4 SSM and lower er-

rors in the winter. However, this advantage may partly reflect the seasonal differences in winter soil-moisture regimes and observation uncertainties (e.g., snow accumulation and freeze–thaw processes) and should therefore be interpreted with caution. In contrast, the DNN performs worse, while the GBM and the DRF are intermediate but more season-dependent, with higher errors in the summer/autumn than in the spring/winter. Overall, relatively lower error levels were observed in the spring and winter, whereas the errors increased moderately in the summer and autumn, highlighting the need for robust modeling strategies under heterogeneous surface and climatic conditions.

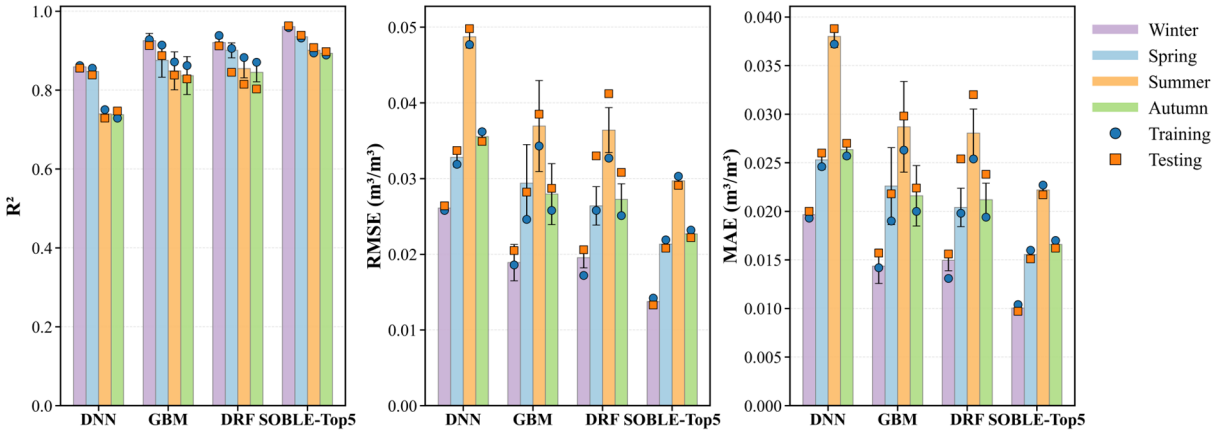


Figure 6. Performance comparison of grouped bar charts for different models with error estimates based on R^2, RMSE, and MAE.

To further interpret the winter performance, we independently examined the snow conditions in the study region using MOD10A1 (Figure 7). After controlling for cloud-induced data gaps with a minimum observation-coverage criterion (ValidFrac $\geq$ 0.1), the regional lower bound of the snow-cover fraction (SnowFrac_LB) exceeded 0.01 on multiple dates, and 10 regional-scale snow events were identified (highlighted by gray shading), most of which were short-lived (1–4 days). These results indicate that the winter soil moisture is likely influenced by snow accumulation–melt processes, under which the surface moisture state and the effective observability/error structure of the SMAP may systematically differ from those in other seasons. Therefore, the lower winter errors are better interpreted as a predictability shift under a specific process regime rather than a universal performance gain under winter conditions. Notably, the snow data were used only for independent verification and discussion support and were not included as an input predictor in the downscaling model (see Appendix A.1 for the data details and the definitions of the derived metrics).

Compared with the original SMAP SSM, all of the downscaling models significantly enhanced the spatial detail representation across Henan Province (Figure 8). The local magnified results indicate that in areas with complex and rugged terrain, such as the Luoyang–Jiaozuo–Zhengzhou region, the DNN model still produces local noise and discontinuous patches. In contrast, the GBM and the DRF, leveraging the inherent structure of the tree-based models, exhibit more a stable performance in suppressing small-scale noise. The SOBLE-Top5 model most accurately reproduces the moisture gradients and the slope-aspect differences in the dry–wet transitional zones of northwestern Henan, showing a superior overall spatial continuity compared to the other models.

In the central-eastern plains (Zhoukou–Zhumadian–Xinyang), the GBM and the DRF effectively capture the heterogeneity of the soil moisture induced by farmland patterns, though local over-smoothing or weakened boundaries remain. SOBLE-Top5, however, preserves both the large-scale trends and the local textures, presenting the most natu-

ral transitions in irrigated areas, high-moisture farmland, and river floodplains, thereby producing a spatial distribution most consistent with the structural characteristics of the original SMAP data.

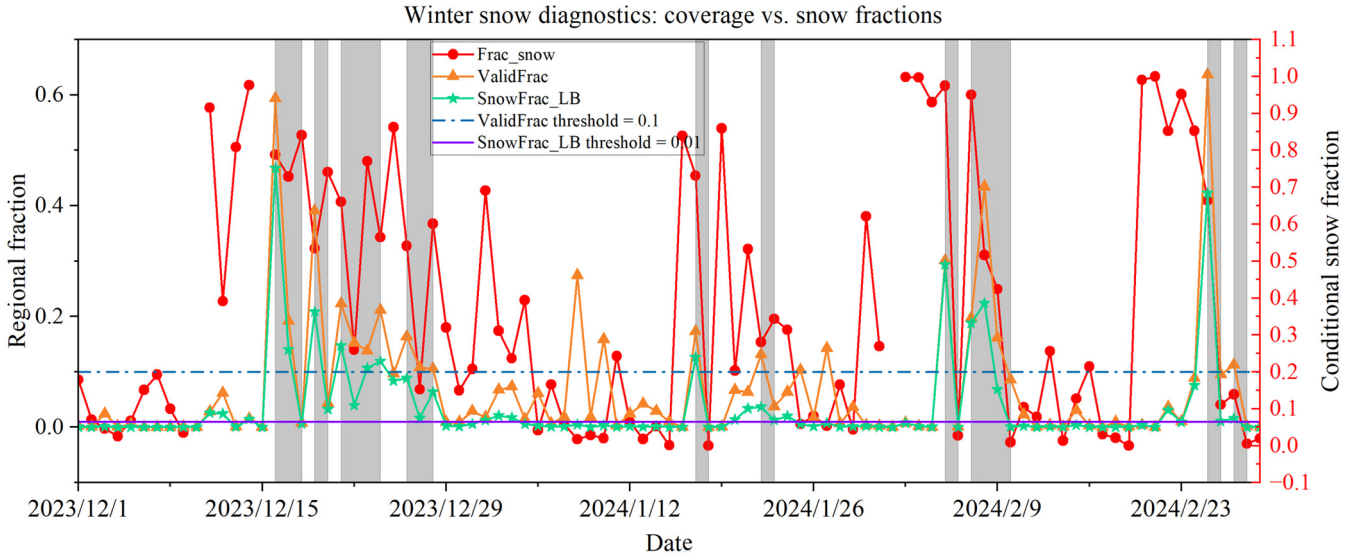


Figure 7. Evidence of winter snow events and observation coverage constraints for interpreting winter model performance.

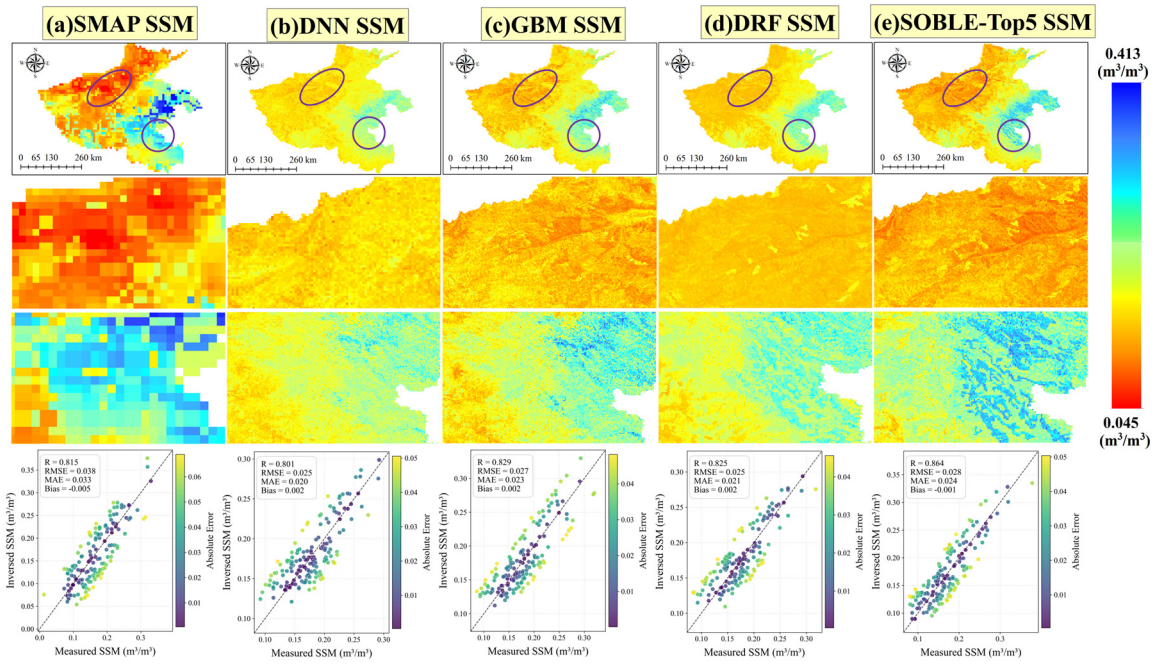


Figure 8. Spatial evaluation of downscaled SSM from 9 km to 1 km resolution using multi-model approaches. (**a**) Original SMAP SSM at 9 km. Panels (**b**–**e**) present the 1 km downscaled SSM derived from DNN, GBM, DRF, and SOBLE-Top5 models, respectively. The second and third rows provide localized zoom-in views to highlight spatial detail enhancement and structural consistency across models. The bottom row shows scatterplots comparing downscaled SSM against reference observations for each method, with associated performance metrics (R, RMSE, MAE, and bias) summarizing model skill and error characteristics.

The ground validation point comparisons further indicate that all of the downscaling models can reasonably reconstruct the SSM, but notable differences exist. The DNN model (R = 0.801) does not substantially improve the accuracy of the SMAP and shows consider-

able scatter in the high-moisture range (>0.25 m^3/m^3), indicating a limited generalization ability under complex surface conditions. By comparison, the GBM and the DRF achieve R = 0.825 and R = 0.829, respectively, outperforming the DNN. Both of the models exhibit stronger clustering of the fitted points in the low-to-medium moisture range (<0.20 m^3/m^3) and more concentrated absolute error distributions. SOBLE-Top5 demonstrates the best performance, attaining the highest correlation coefficient (R = 0.864) and the smallest bias. Its fitted points align most closely with the 1:1 line in the scatter plots, particularly in the high-moisture range of 0.30–0.40 m^3/m^3, with errors significantly lower than those of the other models, indicating its superior capability to stably capture the spatial distribution of the SSM in the study area.

3.4. Stacking Ensemble Downscaling Inversion Results

3.4.1. Comparison of Downscaled SSM Estimates with In Situ SSM

Figure 9 presents a comparison between the SSM estimates from the SOBLE-Top5 seasonal downscaling model and the observed station measurements. To reduce the interference from anomalous weather at the beginning and end of each month, the mid-month date was selected as the representative day for analysis [48]. The model performance was stable in the winter, mainly due to the limited soil moisture variability under frozen conditions. In March and April, the estimated values generally showed good agreement with the observations; however, in May, rapid warming led to abrupt changes in the surface energy conditions, resulting in pronounced SSM fluctuations and a marked decline in the correlation coefficients, indicating the limited ability of the model to respond to rapid hydrothermal variations in the spring. This phenomenon reflects the complex mechanistic characteristics of the spring as a transitional period from frozen to active soil states. Following the termination of freeze–thaw processes, adjustments in the soil pore structure and the water-holding capacity enhance the nonlinearity of the surface soil moisture responses to temperature [49,50]. Meanwhile, rapid vegetation green-up significantly intensifies transpiration, accelerating the surface soil moisture depletion [51] and thereby weakening the model's capability to capture short-term and high-amplitude soil moisture variability during the spring period. Therefore, addressing the complex hydrothermal coupling processes in the spring and the insufficient representation of vegetation physiological dynamics will be a key direction for future model improvements. The accuracy improved in the summer (R = 0.656–0.756), with the largest positive bias (0.023 m^3/m^3) in July due to heavy precipitation. The autumn inversion was optimal and stable, with September achieving the best performance (R = 0.864, RMSE = 0.028).

3.4.2. Time-Series Validation of Downscaled SSM by Land Cover Types

Figure 10 shows the time-series performance of the SOBLE-Top5 SSM across the different land cover types. Overall, SOBLE-Top5 achieves a consistently high accuracy across all of the categories. Built areas perform best (R^2 = 0.80, R = 0.89), outperforming the raw SMAP SSM (R^2 = 0.71, R = 0.84), while crops, trees, and grass maintain a robust temporal agreement ($R \geq 0.73$). The time-series comparison further indicates that SOBLE-Top5 not only preserves the temporal variability of the SMAP SSM but also improves the consistency with the in situ SSM, capturing the seasonal soil moisture evolution. Notably, all of the products respond promptly to precipitation events, showing coherent post-rainfall increases across the land cover types, which supports the physical plausibility and reliability of the downscaling results.

The land cover dependent differences can be explained by surface-condition stationarity and sub-pixel heterogeneity. The superior performance in built-covered areas is likely due to stable surface conditions and consistent impervious surfaces, which reduce the

temporally varying microwave scattering effects and benefit the data-driven downscaling. In contrast, crop-covered areas are affected by phenological stage transitions, potential human management disturbances, and pronounced heterogeneity, making the relationship between the predictors and the SSM more prone to temporal non-stationarity and amplifying the representativeness mismatch between the satellite-scale estimates and the point-based in situ observations. Future improvement over crop-covered areas may be achieved by incorporating explicit phenology, adopting regime-aware modeling by growth stages or hydro-climatic zones, and adding landscape heterogeneity descriptors to better account for mixed pixels.

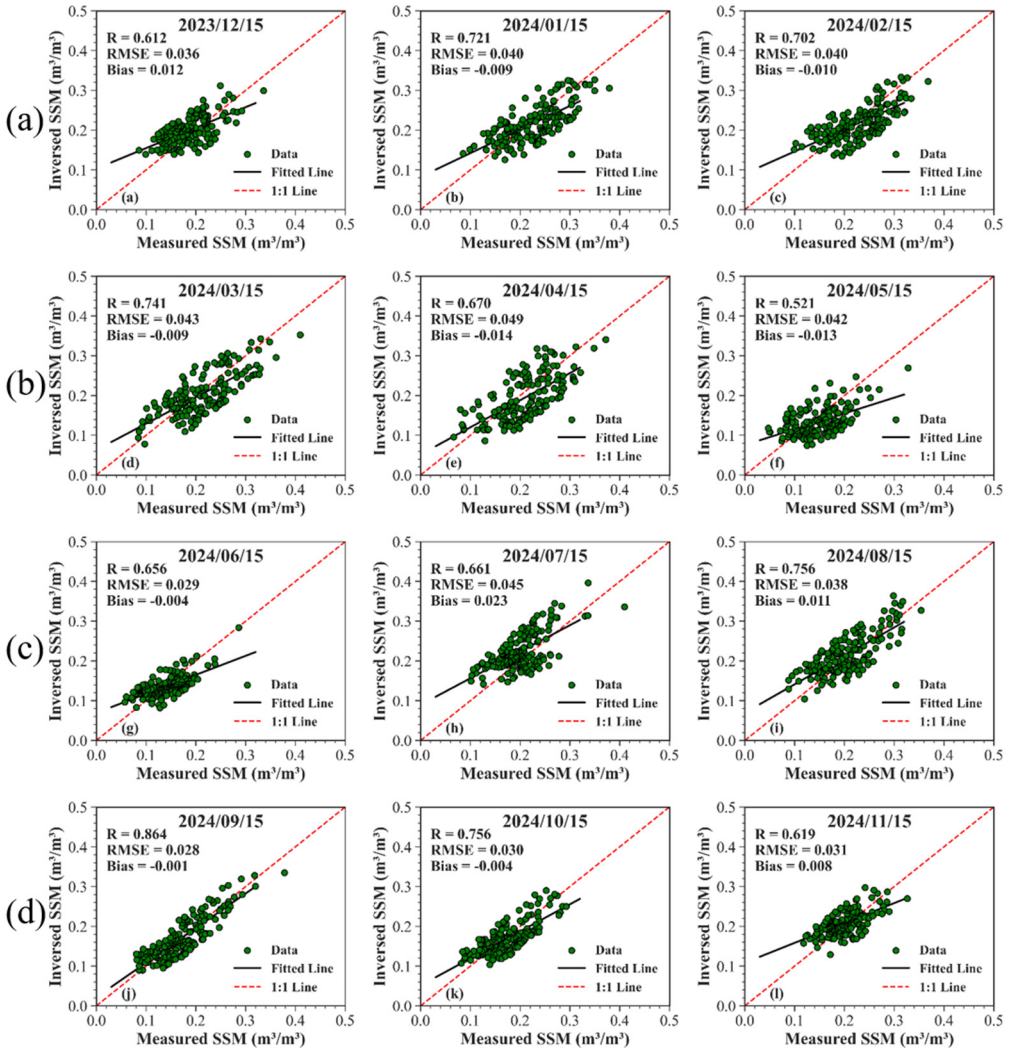


Figure 9. Downscaled SSM estimates and in situ validation using the seasonal downscaling model (SOBLE-Top5). (**a**) winter; (**b**) spring; (**c**) summer; and (**d**) autumn.

The lower correlation in tree-covered areas is consistent with the typical canopy effects in microwave observations: a denser canopy structure and a higher vegetation water content can attenuate the soil moisture signal sensitivity, thereby increasing the retrieval uncertainty and reducing the time-series agreement. Grass-dominated areas exhibit a slightly higher correlation than forests because their canopy structure is simpler and their canopy attenuation is weaker; however, variations in biomass and other residual heterogeneity can still constrain the performance.

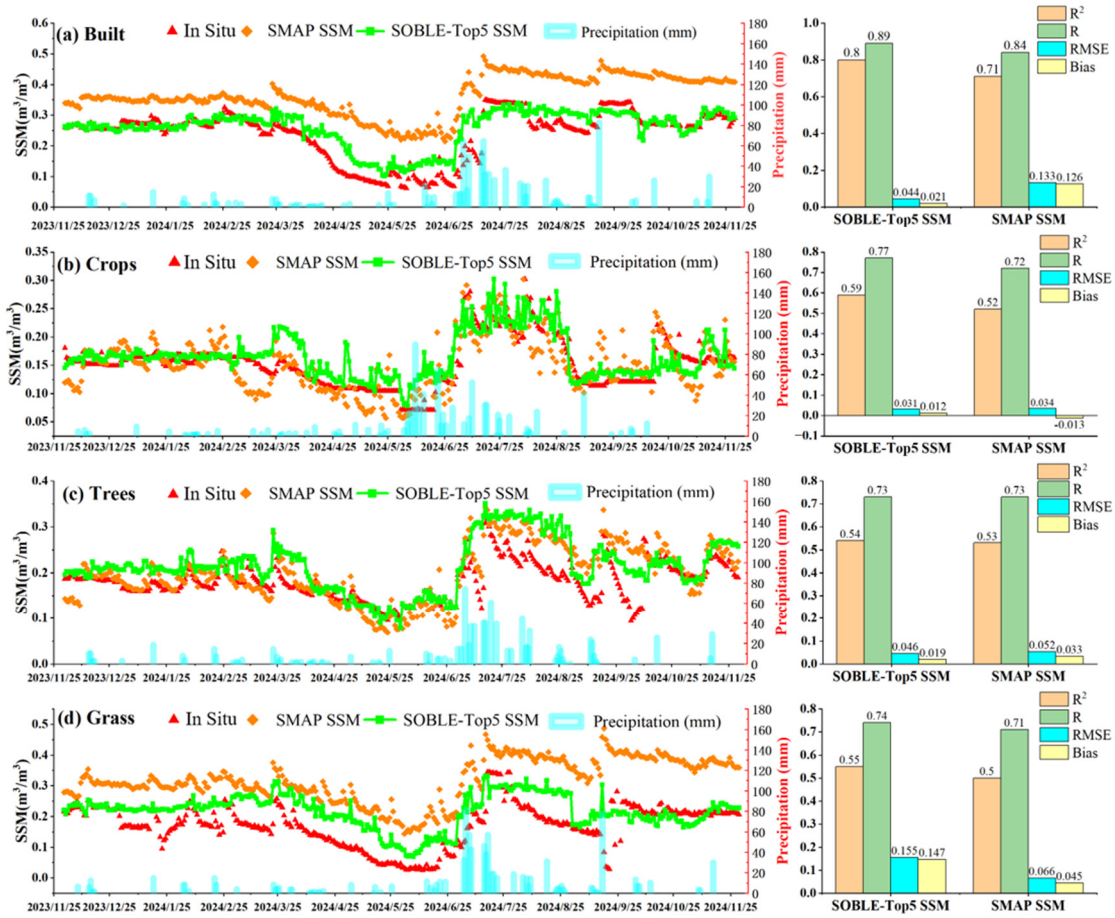


Figure 10. Time-series dynamics of daily precipitation for SOBLE-Top5 SSM, SMAP SSM, and in situ data.

3.4.3. Spatiotemporal Evolution of Downscaled SSM and Its North–South Gradient

Figure 11 presents the spatial distribution of the monthly SSM from December 2023 to November 2024, derived from the proposed downscaling-based inversion. The SSM remained relatively stable in the winter (0.228 m^3/m^3), with localized increases in the southern regions (Xinyang, Zhumadian, and Nanyang) attributable to rainfall and snowfall. In the spring, the northern areas exhibited declines (up to 0.03 m^3/m^3), associated with enhanced evaporative loss, reaching the annual minimum in May–June (mean 0.138–0.136 m^3/m^3), with a localized drought in the northern cities (SSM < 0.08 m^3/m^3). During the flood season (July–August), the SSM increased markedly from the late-spring minimum (0.136 m^3/m^3 in June) to a peak of 0.243 m^3/m^3 in August, with the largest increases in Zhoukou, Shangqiu, Puyang, Zhumadian, and Nanyang (>52%), closely linked to the July rainfall (267–475 mm). In the autumn, the SSM initially stabilized and then increased (September 0.166, October 0.167, November 0.194 m^3/m^3), maintaining a north–south gradient: the southern regions remained wetter, whereas the northern areas (e.g., Anyang and Hebi) stayed relatively dry (<0.18 m^3/m^3). Western Sanmenxia increased by 32.6%, and eastern Zhoukou exhibited the greatest spatial variability (SD = 0.040 m^3/m^3 in November). Overall, the precipitation seasonality and the temperature-related evaporative demand jointly drive these spatiotemporal variations. To strengthen the process-based attribution, future work will stratify the spatial patterns by precipitation–temperature regimes (e.g., threshold-based or clustered hydro-climatic zones) rather than calendar seasons and re-assess both the SSM patterns and the model performance within each regime.

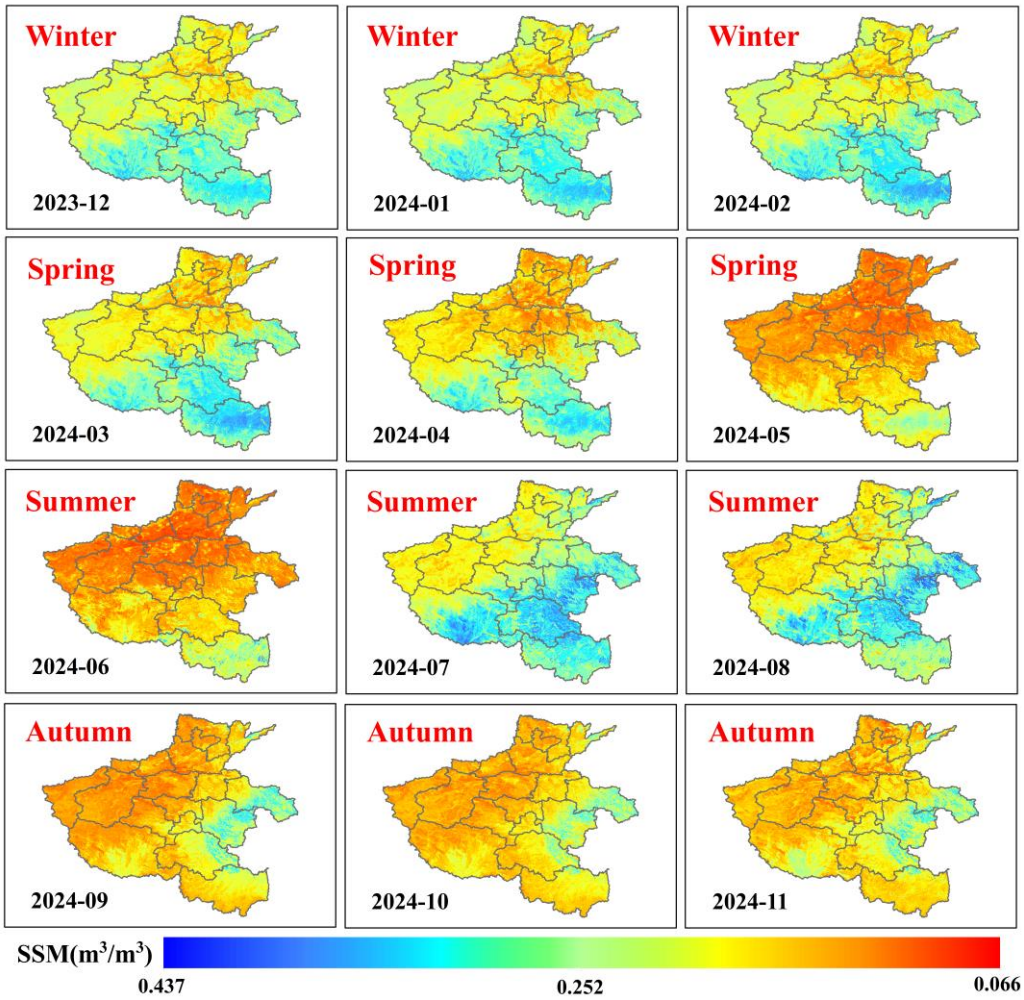


Figure 11. Monthly 1 km downscaled SSM spatial distribution produced by SOBLE-Top5 model.

To examine whether a significant north–south (latitudinal) gradient exists in the spatial distribution of the downscaled SSM across the study region, we performed a monthly quantitative analysis of the SSM–latitude relationship. Since pixel-level samples exhibit a strong spatial autocorrelation that may inflate the statistical significance, we aggregated the downscaled SSM to the prefecture-level city (administrative-unit) scale to obtain a more robust and conservative inference. Specifically, using the period from December 2023 to November 2024, we computed the monthly mean SSM for each of the 18 prefecture-level cities and used each city's representative latitude as the explanatory variable, thereby constructing monthly samples for the subsequent tests of gradient magnitude and significance (see Appendix A.2 for the methodological details).

Across the representative months in each season, the winter and early spring (Figure 12a,b) show a pronounced decline in the SSM with increasing latitude: the Spearman's correlation is significantly negative, and the 95% confidence interval (CI) of the OLS slope b lies entirely below zero, indicating a strong and statistically significant "wetter south–drier north" gradient during this period. In the summer (Figure 12c), the overall gradient remains negative and significant, but the scatter becomes more dispersed, suggesting an enhanced local spatial heterogeneity driven by precipitation processes and land-surface differences. By the autumn (Figure 12d), the absolute slope magnitude decreases markedly; for some months, the CI crosses zero and the correlation becomes non-significant, implying a substantial weakening of the latitudinal gradient. The monthly evolution further supports these findings: Figure 12e shows that $b < 0$ for most months and is often signifi-

cant, but b gradually approaches zero as the season progresses, with non-significant (NS) months emerging in the autumn; Figure 12f shows that the Spearman's ρ remains negative throughout the year, while the $|\rho|$ decreases from larger winter–spring values toward zero, indicating that the north–south moisture gradient weakens from strong to weak over the annual cycle.

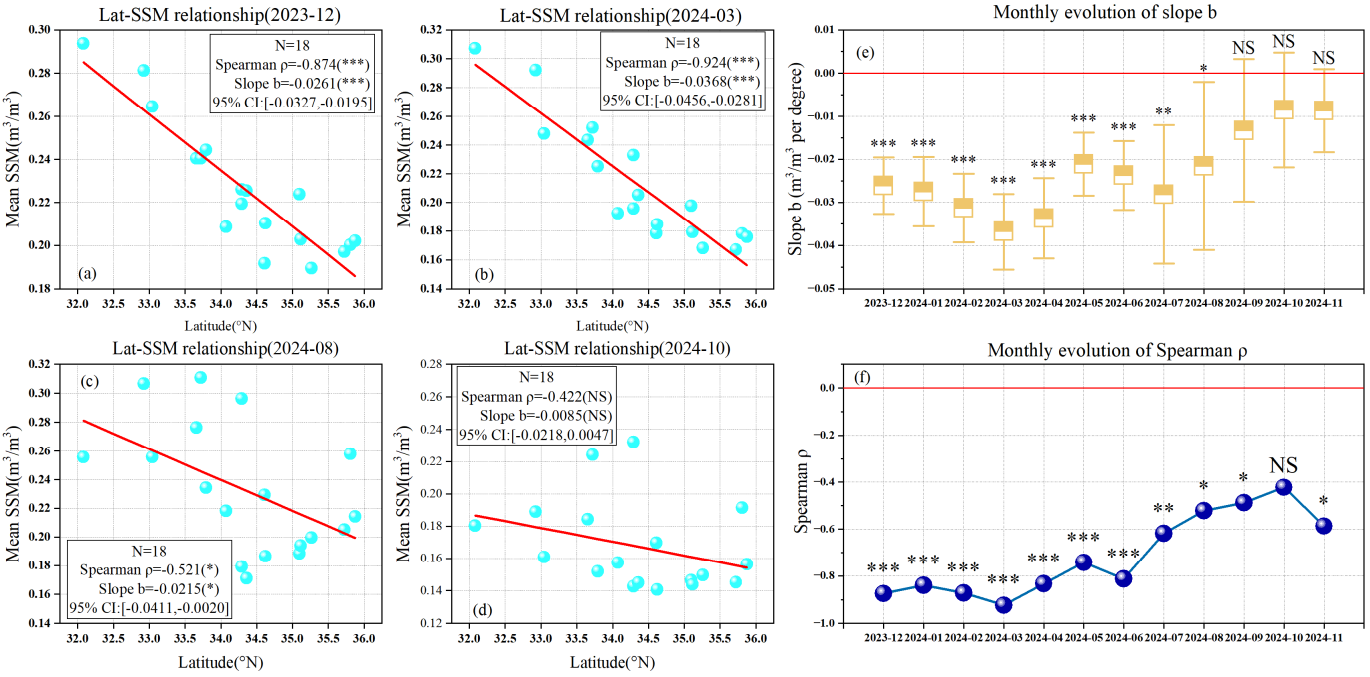


Figure 12. (**a**–**d**) Present the scatterplots and fitted regression lines for representative months, with N, Spearman's ρ, and the regression slope b, together with its 95% CI, annotated within each panel. (**e**,**f**) Show the month-to-month evolution of b and ρ; the red horizontal line denotes y = 0 (the "no-gradient" reference), and asterisks indicate significance levels (* $p < 0.05$, ** $p < 0.01$, *** $p < 0.001$; NS denotes not significant).

Figures 13 and 14 present the decadal spatial distribution and temporal dynamics of the SSM in Henan Province from March to July. The results reveal a persistent expansion of low SSM regions during March–May, predominantly distributed across the northern, central, and eastern plains. The period from May to early June corresponds to the most pronounced expansion of low SSM areas, with the minimum values reaching 0.05 m^3/m^3. The quantitative analysis indicates that the area affected by a moderate drought (SSM < 0.15 m^3/m^3) increased substantially from 7120 km^2 in late March to 95885 km^2 in late May, attaining its peak within this interval. The severe drought areas (SSM < 0.10 m^3/m^3) exhibited a rapid increase from mid-April to early June, reaching a maximum of 28974 km^2 in early June. Following mid-June, the drought-affected areas of all severity levels exhibited a gradual contraction. By July, the regions with a high SSM re-expanded in southern Henan and the western mountainous areas, whereas the residual low-value zones persisted in northern and central Henan.

The results illustrated in Figure 15 indicate pronounced spatial heterogeneity in the downscaled SSM across Henan Province. Overall, relatively low SSM levels are observed in the central–northern region, with minimum values of approximately 0.05 m^3/m^3, whereas the central–southern and southern regions exhibit substantially wetter conditions. In these areas, high and low value patches are interwoven, forming clearer spatial gradients. Such spatial contrasts are primarily governed by the combined effects of soil physicochemical properties and underlying surface conditions. As the main grain-producing area of the study region, the central–northern plain of Henan is characterized by extensive cropland

and a relatively high sand content, resulting in a limited soil water-holding capacity. Consequently, the SSM remains generally low and is more sensitive to variations in precipitation and evapotranspiration, implying a higher risk of agricultural drought. In contrast, the central–southern and the southern regions exhibit a higher clay content and better vegetation cover, which enhance the soil moisture retention and lead to higher overall SSM levels with a stronger spatial continuity. Across cropland areas, the NDVI shows a significant positive correlation with the SSM, indicating that higher soil moisture availability is conducive to crop growth and reflecting a coupled vegetation–soil moisture dynamic. However, in areas along the Middle Route of the South-to-North Water Diversion Project and within the Yellow River Basin, regions with a relatively high NDVI but low SSM are observed, which can likely be attributed to anthropogenic water regulation practices such as irrigation. This highlights the important role of human activities in shaping agricultural soil moisture patterns. By comparison, built-up areas and bare land consistently exhibit low SSM values. Overall, the downscaled SSM demonstrates a strong physical consistency and a regional representativeness in its spatial distribution, providing a reliable data basis for agricultural water status assessment and agricultural drought risk analysis.

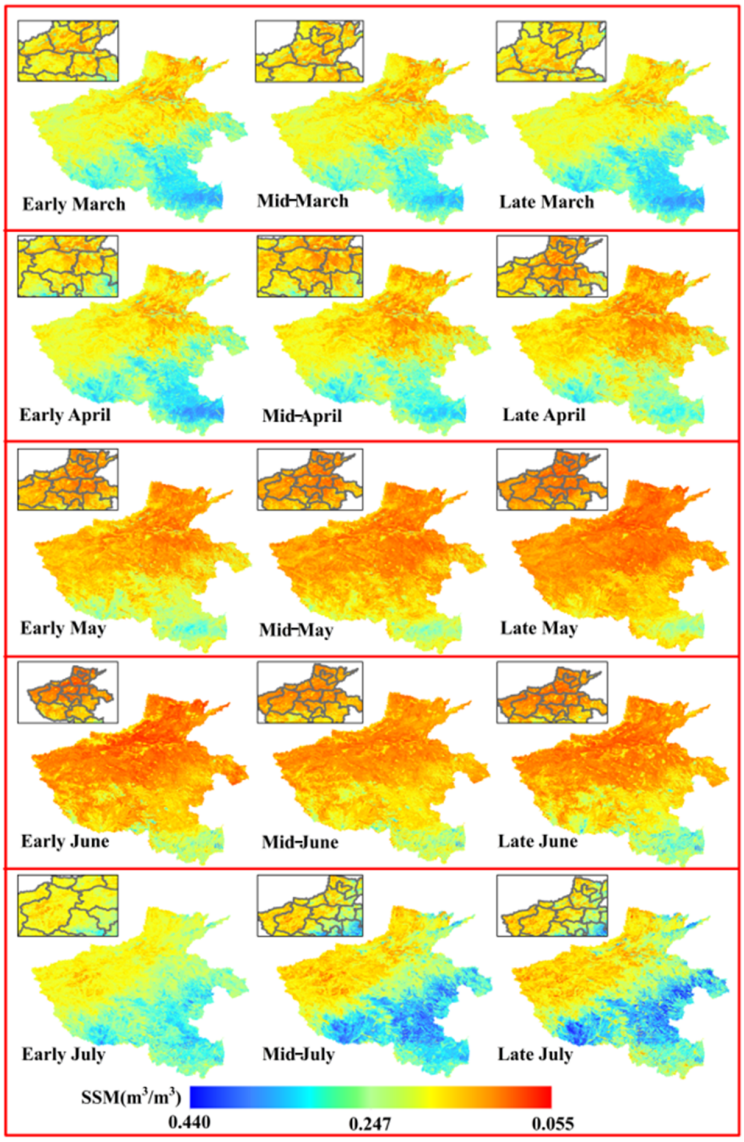


Figure 13. Decadal spatial distribution of downscaled SSM from March to July.

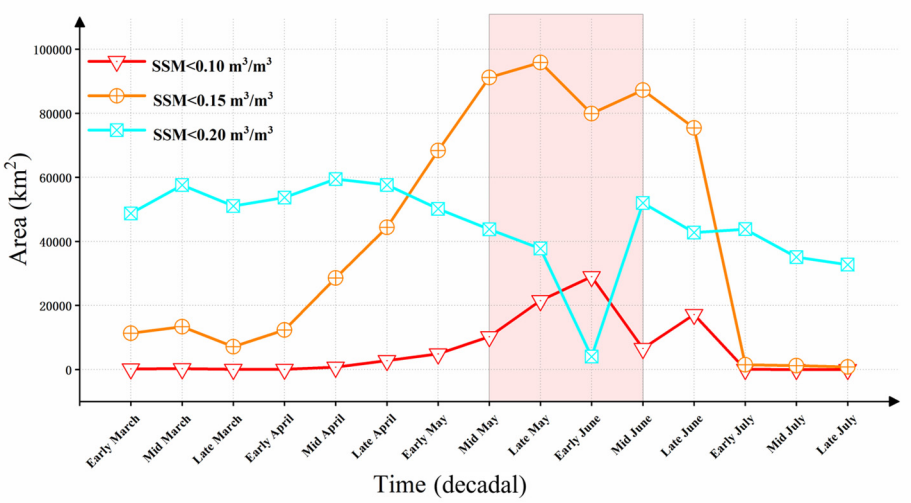


Figure 14. Changes in drought area at different SSM thresholds at the decadal scale. The shaded area in the figure represents the period of severe drought from mid-May to early June, during which SSM decreased significantly.

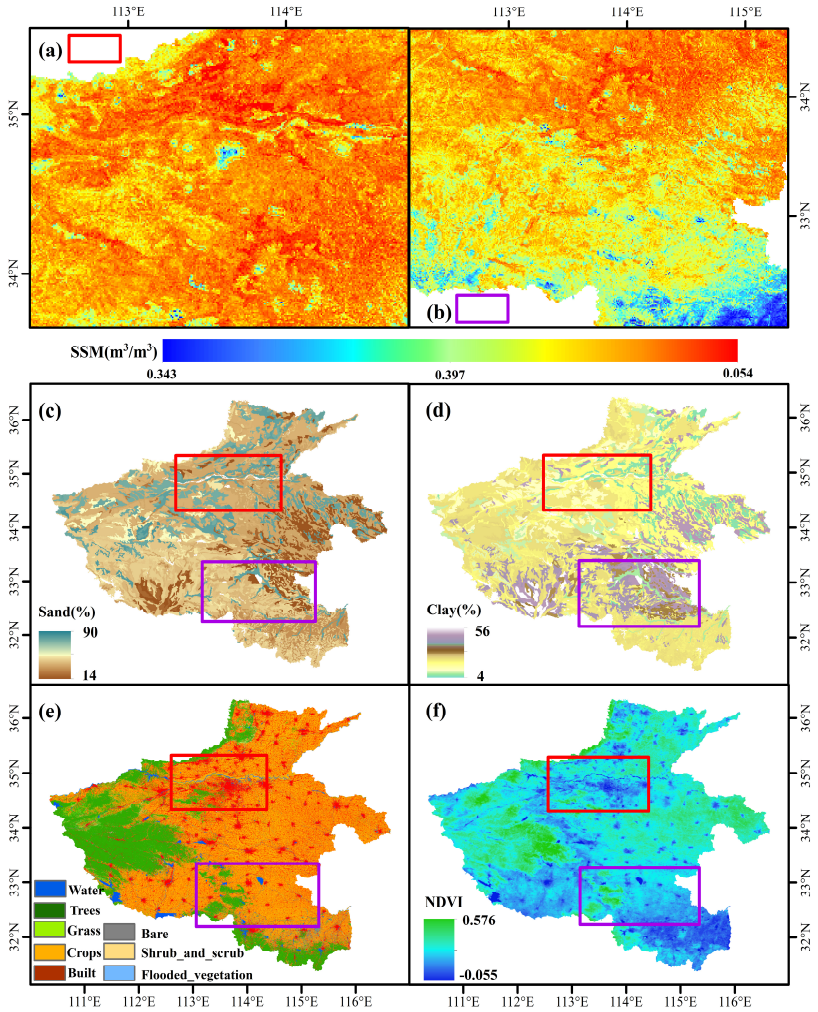


Figure 15. (**a**) Downscaled SSM results for the selected central–northern Henan region; (**b**) downscaled SSM results for the selected central–southern Henan region; (**c**) spatial distribution of sand content; (**d**) spatial distribution of clay content; (**e**) land cover classification map; and (**f**) Normalized Difference Vegetation Index (NDVI) classification map.

3.5. Dynamic Contribution of Driving Factors

To enhance the model interpretability and identify the key drivers influencing the SSM variations, the SHAP (SHapley Additive exPlanations) method [52] was employed. This approach, grounded in game theory principles, quantifies each input factor's impact on the model predictions by calculating the average marginal contribution of each feature across all of the possible combinations. The SHAP simultaneously provides global importance rankings and local explanations for the individual samples. In this study, the SHAP values were calculated for each driver of the SOBLE-Top5 model to reveal differences in the variable contributions and the influence on the directions across the seasons. Positive and negative SHAP values indicate the promoting and inhibiting effects of variables on the SSM, respectively. This method facilitates the physical mechanism-level analysis of how multi-source environmental factors drive surface soil moisture dynamics.

Figure 16 illustrates the SHAP summary analysis, which systematically reveals the relative importance of the driving factors of the SSM and their underlying mechanisms across the different seasons. The results indicate that soil properties, topographic conditions, and vegetation–energy factors jointly control the seasonal spatial variability of the SSM. Among them, soil bulk density and clay content exhibit markedly higher mean |SHAP| values in the winter and spring, identifying them as the dominant factors governing cold-season soil moisture patterns. Specifically, soil bulk density shows a clear threshold effect at approximately 1.39–1.55 g/cm^3: when the bulk density is below this range, the SHAP values are predominantly positive, indicating that looser soils possess a greater capacity for water storage; once the bulk density exceeds the threshold, the SHAP values rapidly shift to negative and become more variable, reflecting the adverse effects of compacted soils on infiltration and water retention. Clay content maintains a high contribution throughout all of the seasons, and the SHAP values become distinctly positive when the clay content exceeds approximately 21%, suggesting that clay-rich soils are more capable of sustaining higher near-surface moisture levels under precipitation or irrigation inputs.

With respect to topographic factors, elevation exhibits a stable and physically consistent influence across all of the seasons, with its importance particularly pronounced in the summer and autumn. The SHAP dependence plots indicate that low-elevation areas (<200 m) are generally associated with positive SHAP values, whereas the SHAP values turn negative with increasing elevation, highlighting the integrated regulation of evapotranspiration demand and soil moisture retention along terrain–climate gradients. The slope shows an overall negative effect in the spring and autumn, with the spring being especially sensitive, reflecting the amplification of soil moisture deficits on steeper slopes under limited precipitation and enhanced runoff generation. Vegetation and energy-related factors primarily regulate the SSM through evapotranspiration processes. The NDVI displays a consistent piecewise response across all of the seasons: when the NDVI < 0, the SHAP values are strongly positive, mainly characterizing high-moisture land-surface types such as water bodies, snow cover, or wet bare soils; when the NDVI > 0, the SHAP values are generally weakly negative, indicating that in the study area—dominated by cropland and low-stature vegetation—the net regulatory effect of vegetation on the near-surface soil moisture is limited. The LAI exhibits a pronounced threshold effect in the spring (around 0.8), whereby low-to-moderate vegetation cover suppresses evaporation and enhances soil moisture conservation, whereas at higher LAI levels, transpiration losses become dominant. The LST emerges as the most critical negative driver in the spring and summer, with clear inflection points at approximately 23–24 °C (spring) and 31 °C (summer); beyond these thresholds, intensified evapotranspiration leads to a sharp decline in the SSM, clearly depicting the classical "warming–drying" process. Although the influence of the LST weakens in the autumn, it still exhibits a bimodal nonlinear response. In addition, summer

precipitation contributes positively and significantly to the SSM, while the Albedo-VIS shows moderate importance in the summer and autumn, reflecting its indirect indication of the soil moisture background under relatively stable vegetation conditions.

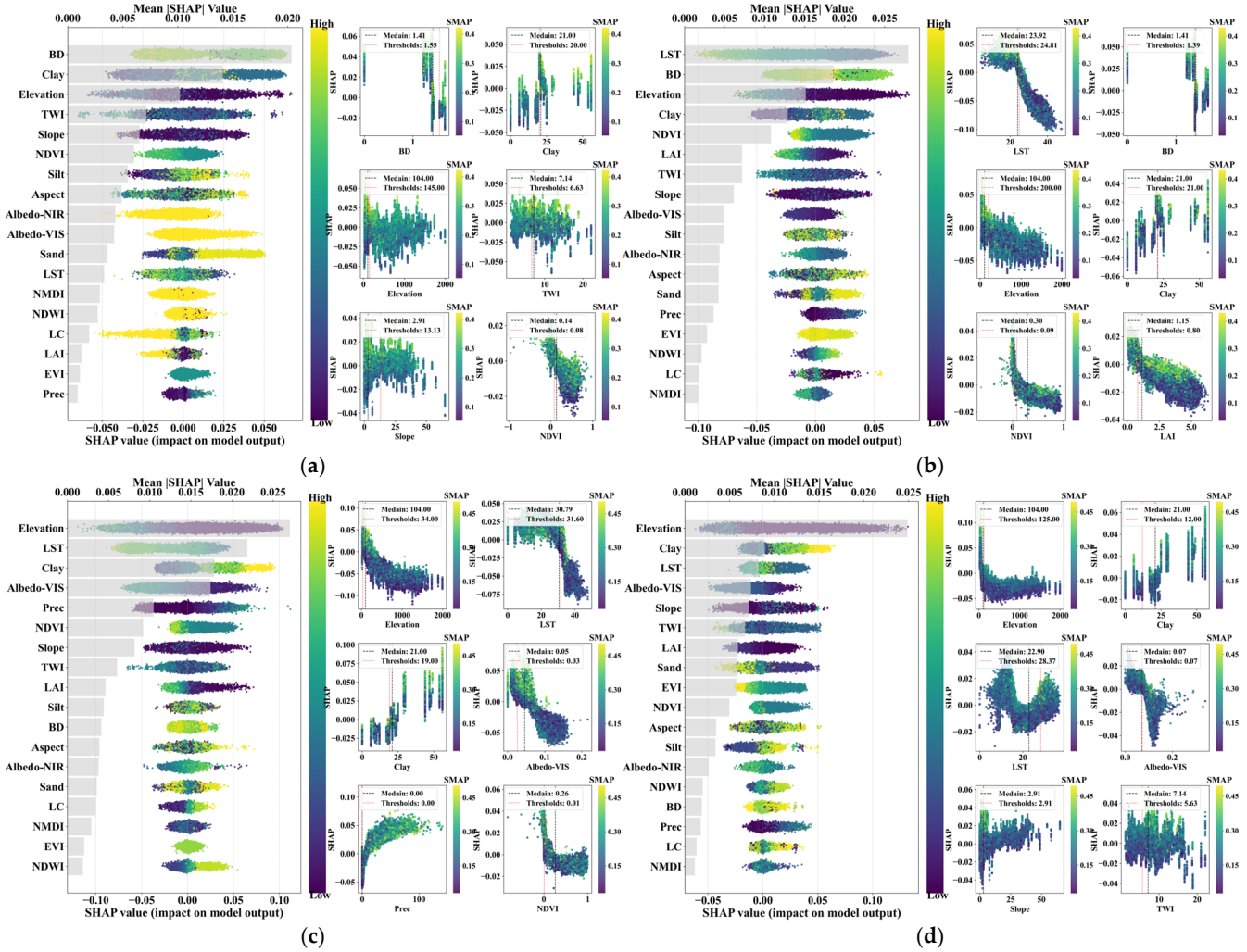


Figure 16. Summary plot of SSM driver contributions across seasons: (**a**) winter; (**b**) spring; (**c**) summer; and (**d**) autumn.

Figure A1 illustrates the SHAP-based heatmap showing the distribution of the primary drivers across the four seasons, highlighting the directionality and the spatial heterogeneity of their effects on the SSM. Red represents positive contributions, whereas blue denotes negative effects. Overall, the dominant drivers exhibit a seasonal shift from soil-structure-related factors in the cold seasons toward vegetation–energy- and precipitation-related factors in the warm seasons, with topographic constraints becoming more evident in the late summer and autumn.

Building upon the SHAP main-effect analysis, we further computed the SHAP interaction values and used the mean absolute interaction strength (mean |SHAP interaction|) to characterize the nonlinear synergies among the predictors. Figure 17 presents the interaction-strength heatmaps for the winter, spring, summer, and autumn. Specifically, in the winter, the interactions among soil property-related factors (e.g., Clay and BD) are particularly pronounced, consistent with the dominant role of soil structural characteristics in water retention and transfer under freezing or near-freezing conditions. In the spring and summer, the interactions between the vegetation state indicators (EVI/NDVI) and the surface energy indicators (LST) are notably stronger, indicating that the coupling between

vegetation transpiration and surface energy processes has a significant influence on surface soil moisture dynamics. In the autumn, the relatively strong interactions among topographic factors (e.g., elevation and aspect) reflect the enhanced effects of the topography on radiation distribution and water redistribution, contributing to the spatial heterogeneity of the soil moisture.

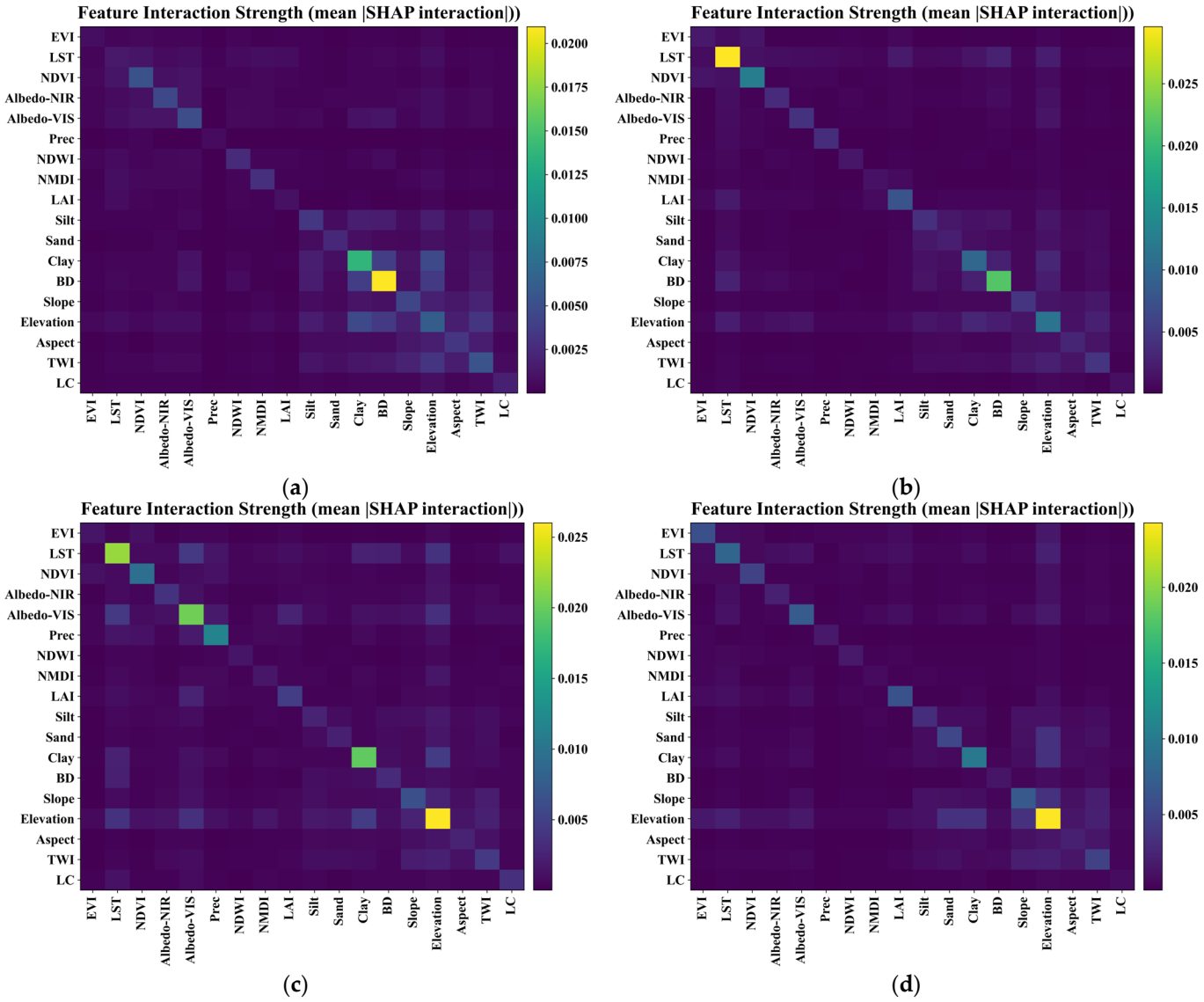


Figure 17. Seasonal SHAP interaction strength heatmaps (mean |SHAP interaction|) for key drivers of SSM: (**a**) winter; (**b**) spring; (**c**) summer; and (**d**) autumn.

Moreover, the season-dependent interaction patterns among the environmental factors not only provide a more comprehensive framework for interpretation but also offer practical implications. For instance, in the winter, recognizing soil property-dominated interactions can improve the soil moisture estimation under freezing conditions; in the spring and summer, identifying the effects of vegetation–surface energy–climate coupling can help optimize the downscaling models for soil moisture prediction under changing meteorological conditions; and in the autumn, topography-driven interaction patterns can guide water resource management strategies at field or watershed scales, thereby enhancing the applicability of the downscaled soil moisture products for agricultural and ecological management.

3.6. Uncertainty and Sensitivity Analysis

3.6.1. Comparative Analysis of Same-Day Precipitation and Antecedent Precipitation Indices

To clarify the role of precipitation temporal information (i.e., "memory effects") in the downscaling framework, we conducted a sensitivity analysis in which the seasonal grouping, train/test split, model architecture, and hyperparameter settings were kept unchanged, and only the precipitation-related predictors were replaced with P14 and API090 (see Appendix A.3 for their definitions), with the results summarized in Table 4. The baseline configuration uses same-day precipitation on the SMAP overpass date (P_0), which achieves consistently high accuracy across all of the seasons in the test set (R^2 = 0.8977–0.9632; RMSE = 0.0133–0.0291 m^3/m^3), indicating that same-day precipitation alone can stably capture the dominant precipitation input signal for the SSM. In contrast, the simple cumulative precipitation metric P_{14} shows clear season-dependent benefits: although the summer test RMSE decreases from 0.0291 to 0.0278 m^3/m^3, the performance slightly deteriorates in the winter and autumn (winter: RMSE increases from 0.0133 to 0.0134 m^3/m^3; autumn: RMSE increases from 0.0222 to 0.0228 m^3/m^3), suggesting that a fixed-window accumulation does not yield consistent improvements across seasons. The exponentially decayed antecedent precipitation index (API090) provides more consistent gains in the spring and autumn (e.g., spring test RMSE decreases from 0.0208 to 0.0191 m^3/m^3; autumn: RMSE decreases from 0.0222 to 0.0200 m^3/m^3), but it requires additional parameter choices such as the decay factor and look-back window (see Appendix A.3), whose transferability may depend on the regional hydro-climatic conditions. From a process perspective, the SMAP surface soil moisture is more sensitive to near-term precipitation inputs, while longer-term "memory effects" can be partially and implicitly represented through covariates related to temperature-driven evaporative demand (e.g., LST/ET-related variables), vegetation state, and land-surface properties. Therefore, adopting P_0 as the default precipitation predictor provides a stable and reliable downscaling performance while maintaining model parsimony and transferability.

Table 4. Sensitivity of downscaling performance to precipitation temporal representation across seasons (test set only).

Precipitation Setting	Evaluation Indicators	Winter	Spring	Summer	Autumn
P0	R^2	0.9632	0.9389	0.9078	0.8977
	RMSE	0.0133	0.0208	0.0291	0.0222
	MAE	0.0097	0.0151	0.0217	0.0167
P14	R^2	0.9676	0.9401	0.9243	0.9010
	RMSE	0.0134	0.0206	0.0278	0.0228
	MAE	0.0098	0.0150	0.0208	0.0167
API090	R^2	0.9678	0.9481	0.9122	0.9165
	RMSE	0.0125	0.0191	0.0283	0.0200
	MAE	0.0098	0.0139	0.0214	0.0145

RMSE and MAE are expressed in units of m^3/m^3.

3.6.2. Quantifying Depth-Mismatch Bias in Validation

To quantify the potential systematic bias introduced by the depth mismatch between the SMAP near-surface SSM (5 cm) and the in situ measurements at 10 cm, we conducted a scenario-based sensitivity analysis based on the full-period daily 10 cm in situ observations used for validation. Using the 10 cm observations as the baseline ($\Delta = 0$), we constructed a "5 cm-like" reference series as SM5 = SM10 $\pm$ Δ, where Δ = 0.01 and 0.02 m^3/m^3 represent plausible scenarios in which the near-surface layer is relatively wetter (+Δ) or drier ($-\Delta$) than the 10 cm layer. For each scenario, the validation metrics (bias and RMSE) were recalculated between the predictions and the reference series. The results (Figure 18) show that bias responds to Δ in an approximately 1:1 linear manner, indicating that the

depth mismatch primarily manifests as an additive systematic offset. Under the baseline (10 cm) scenario, the bias is -8.60×10^{-5} m^3/m^3, which is negligible. When $\Delta = \pm 0.01$, the bias becomes -0.01009 and $+0.00991$ m^3/m^3, respectively; when $|\Delta| = 0.02$, the bias reaches -0.02009 and $+0.01991$ m^3/m^3, implying an upper bound of approximately 0.02 m^3/m^3 for the systematic bias attributable to reasonable depth differences. In contrast, the RMSE is less sensitive to Δ and exhibits a shallow U-shaped pattern: the baseline RMSE is 0.05142 m^3/m^3; it increases only to 0.05237–0.05240 m^3/m^3 when $|\Delta| = 0.01$, and it reaches a maximum of 0.05521 m^3/m^3 when $|\Delta| = 0.02$ (an increase of 0.00378 m^3/m^3, about 7% of the baseline RMSE). Overall, these results indicate that the depth mismatch affects the error statistics mainly through a systematic offset, while its impact on the overall error magnitude is comparatively limited, thereby providing a quantitative uncertainty bound for the validation conclusions in this study.

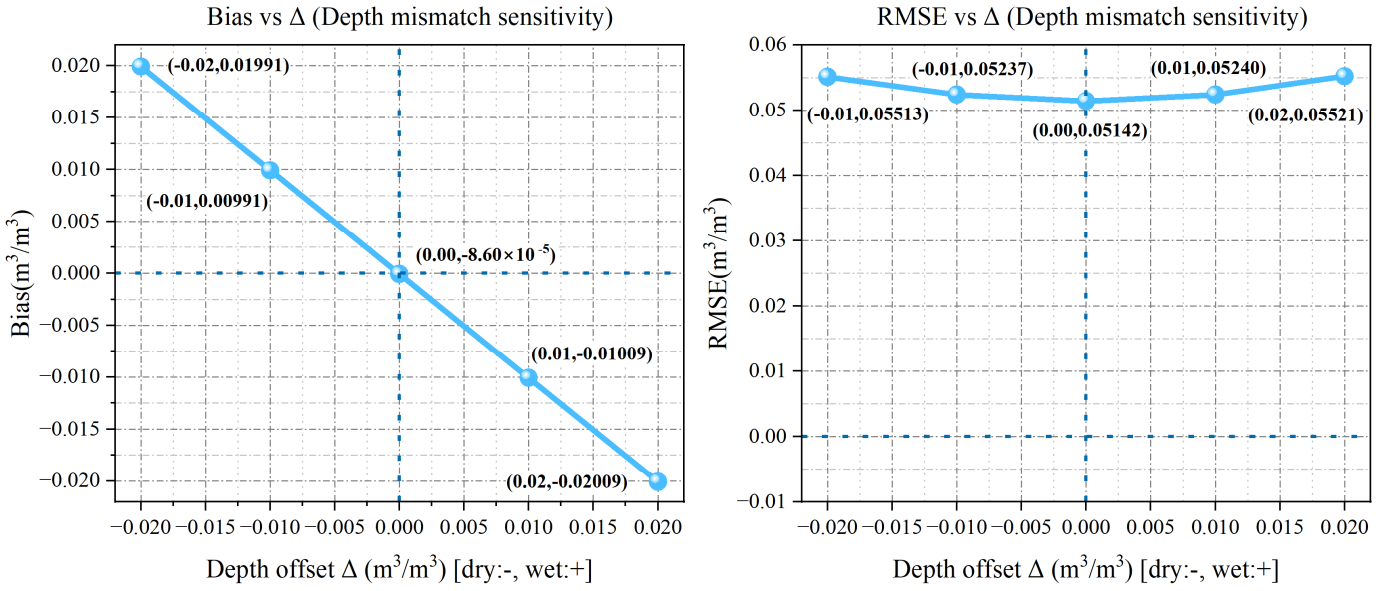


Figure 18. Sensitivity of validation metrics to depth mismatch (5 cm vs. 10 cm).

4. Discussion

1. Since snow observations during the study period were substantially affected by winter cloud-induced data gaps, the winter model is limited by the lack of explicit snow-related predictive variables. Therefore, the lower winter errors are more likely to reflect changes in "predictability" under specific physical states rather than an inherently superior model performance in the winter. In future work, we will incorporate physically meaningful proxies of freeze–thaw and snow processes (e.g., temperature-threshold freeze–thaw indicators, snow cover or snow water equivalent) and conduct stratified evaluations under frozen vs. unfrozen (or snow-covered vs. snow-free) conditions to improve the winter process consistency and the model interpretability.
2. Resampling the multi-source driving factors to 9 km ensures consistency with the SMAP target scale, but it inevitably smooths sub-pixel heterogeneity and leads to a loss of fine spatial details. In future work, we will mitigate this scale-induced bias by incorporating multi-scale statistical/texture descriptors at the 9 km sample-construction stage (e.g., mean, standard deviation, and terrain relief) and by adopting aggregation schemes that are consistent with the physical properties of each variable. Meanwhile, we will explore a two-stage residual-refinement framework: first learning a scale-consistent background field at 9 km and then refining the residuals during inference using 1 km predictors to improve the local consistency and physical realism

of the 1 km products. Importantly, the forthcoming NISAR soil moisture products at 200 m resolution can serve as an independent high-resolution reference for field-scale validation and for introducing cross-scale consistency constraints, thereby enabling a more systematic assessment and reduction of scale-dependent errors.

3. This study was trained and validated only in Henan Province; therefore, the transferability of the derived model parameters and performance conclusions to other climate zones or geomorphic settings remains uncertain. Although the proposed seasonal ensemble downscaling framework is methodologically generic and mainly relies on widely available remote sensing and meteorological driving variables, applying it to other regions typically requires re-training and/or calibration using representative samples from the target region. In particular, in permafrost or strong freeze–thaw regions of Northeast China, snow cover and freeze–thaw processes can substantially alter winter soil-moisture dynamics and microwave observability, potentially causing domain shifts in the predictor–SSM relationships; thus, its applicability should be further assessed through dedicated cross-regional validation.
4. Taking winter as an example, we evaluated the performance–efficiency trade-off under different ensemble strategies and ensemble sizes. The results show that, as the number of base learners increases, the training time generally exhibits an upward trend; meanwhile, compared with a single model or a smaller-scale ensemble, the model performance improves in most settings, but some strategy–size combinations may experience diminishing marginal gains or even performance degradation (see Table A3). Future work will systematically assess the joint optimum among "performance–latency–resource" for operational deployment and further improve the runtime efficiency by integrating model compression and dynamic ensemble strategies.

5. Conclusions

This study systematically assessed the effects of seasonal modeling, model architecture, and multi-source drivers on SMAP SSM downscaling and inversion. The results indicate that seasonal modeling markedly outperforms the all-season approaches, with the SOBLE-Top5 model achieving the highest accuracy and finest spatial detail. The SSM exhibits pronounced spatiotemporal variability, primarily governed by meteorological conditions, topography, and soil texture. These findings improve the accuracy and physical interpretability of SSM estimates and provide high-resolution products to support regional drought monitoring, agricultural management, and water resource planning.

The main conclusions are as follows:

(1) This study examined seasonal and all-season modeling strategies, with the results indicating that seasonal modeling demonstrated superior overall performance. The winter ET and RF models achieved R^2 values of 0.9493 and 0.9479, respectively, representing improvements of approximately 9–14% and reductions in the RMSE of about 47–50%. The seasonal modeling more accurately captures the dynamic response relationship between environmental factors and soil moisture.

(2) The SOBLE-Top5 model achieved superior performance in the seasonal SSM downscaling inversion. Compared with the best single base learner, it improved the R^2 by 0.98–4.65% and reduced the RMSE by 9.30–21.22%. Across all of the seasons, SOBLE-Top5 maintained the highest accuracy (R^2= 0.9389–0.9632), consistently outperforming the GBM, DRF, and DNN models, with the DNN showing the weakest results (R^2 = 0.7290–0.8556). These findings confirm that multi-source data integration and hierarchical ensemble learning significantly enhance the prediction accuracy and seasonal adaptability for high-resolution moisture estimation.

(3) The SSM in the study area exhibited pronounced spatiotemporal variability. It remained relatively stable in the winter, declined slightly in the northern regions during the spring due to enhanced evapotranspiration, and reached its annual minimum in May–June (SSM < 0.08 m^3/m^3). During the July–August flood season, the SSM rapidly increased following heavy rainfall, with local rises exceeding 52%. In the autumn, the SSM stabilized before gradually increasing, with consistently higher values in the south, revealing a distinct north–south gradient. Meanwhile, the decadal analysis from March to July demonstrates a clear evolutionary pattern in which the low-SSM areas continuously expand throughout the spring, reach their maximum extent during May–June, and then contract markedly in July in response to improved moisture conditions.

(4) The driving mechanisms of SSM exhibit pronounced seasonal variability. In the winter, the SSM is primarily governed by physical properties such as BD and clay content, resulting in relatively stable soil moisture levels. In the spring, the SSM is largely influenced by the negative effects of the LST, combined with the controlling effects of elevation and soil texture [53]. During the summer and autumn, multiple factors—including elevation, temperature, precipitation, and soil texture—jointly regulate the SSM, with summer precipitation exerting the most significant impact on the instantaneous SSM variations [54].

Author Contributions: All the authors made significant contributions to this work. Conceptualization, S.Z. and H.Y.; methodology, S.Z. and H.Y.; software, Q.L.; data curation, S.Z. and B.J.; supervision, H.Y. and D.P.; validation, B.J.; visualization, Q.L.; writing—original draft preparation, S.Z. and D.P.; writing—review and editing, H.Y. and S.Z. All authors have read and agreed to the published version of the manuscript.

Funding: This research was funded by the National Natural Science Foundation of China (U1304402, 41977284) and the Laboratory of Mine Spatio-Temporal Information and Ecological Restoration, MNR (No.KLM202310).

Data Availability Statement: The datasets generated and analyzed during this study are available from the corresponding author on reasonable request.

Conflicts of Interest: The authors declare no conflicts of interest regarding the publication of this manuscript.

Appendix A

Appendix A.1. Snow Cover Screening and Coverage-Constrained Indicators

This study used the MODIS Terra daily snow product MOD10A1 Collection 6.1 (500 m spatial resolution) to characterize winter snow conditions in the study region, with the NDSI_Snow_Cover band (0–100) selected as the snow-cover variable. For quality control, only valid values within 0–100 were retained, while all other special codes (e.g., cloud, night, and missing) were treated as missing values. The detailed definitions, threshold settings, and calculation formulas of these indicators are provided below.

(1) Observation coverage fraction (ValidFrac):

$$\text{ValidFrac} = \frac{n_{\text{valid}}}{N_{\text{total}}} \tag{A1}$$

where n_{valid} denotes the number of pixels within the study area with valid observations on that day, and N_{total} denotes the total number of pixels in the study area.

(2) Conservative lower-bound regional snow fraction (SnowFrac_LB):

$$\text{SnowFrac_LB} = \frac{n_{\text{snow}}}{N_{\text{total}}} \tag{A2}$$

where n_{snow} is satisfying the number of pixels (i.e., snow cover $\geq 40\%$). Since the denominator is N_{total} and missing pixels are effectively treated as "non-snow," this metric provides a conservative regional lower bound of snow-cover fraction.

(3) Conditional snow fraction over the visible area (Frac_snow):

$$\text{Frac_snow} = \frac{n_{\text{snow}}}{n_{\text{valid}}} \tag{A3}$$

which is computed only over the visible (valid observation) area and represents the conditional snow fraction. It is used to aid interpretation on low-coverage days where snow may be present only within the observed subset.

Appendix A.2. Spearman and OLS-Based Quantification of Latitudinal SSM Gradients

Specifically, for each month m (December 2023 to November 2024), the downscaled SSM was aggregated to 18 prefecture-level cities. Let $i \in \{1, \ldots, 18\}$ denote the city index. The mean SSM for city i in month m is defined as follows:

$$SSM_{i,m} = \frac{1}{\mid \Omega_i \mid} \sum_{\mathbf{x} \in \Omega_i} SSM_m(\mathbf{x}) \tag{A4}$$

where Ω_i is the set of pixels within the administrative boundary of city i, $\mid \Omega_i \mid$ is the number of pixels, and $SSM_m(\mathbf{x})$ is the monthly downscaled SSM at location $\mathbf{x}$. A representative latitude ϕ_i (°N) was assigned to each city based on the centroid of the administrative unit, yielding the monthly sample set

$$\mathcal{D}_m = \{(\phi_i, SSM_{i,m})\}_{i=1}^{18} \tag{A5}$$

On this basis, two complementary tests were used to characterize the latitudinal gradient.

(1) Spearman rank correlation. For each month m, the Spearman rank correlation coefficient between $SSM_{i,m}$ and ϕ_i was computed:

$$\rho_m = \text{corr}\ (\text{rank}(SSM_{i,m}),\ \text{rank}(\phi_i)) \tag{A6}$$

where $\mid \rho_m \mid$ quantifies the gradient strength and $\rho_m < 0$ indicates that SSM decreases with increasing latitude (i.e., a south-to-north drying tendency). Statistical significance was evaluated using a two-sided test with p-value $p_{\rho,m}$ and denoted as * ($p < 0.05$), ** ($p < 0.01$), and *** ($p < 0.001$); NS indicates not significant ($p \geq 0.05$).

(2) OLS regression slope. To obtain a physically interpretable estimate of gradient magnitude, an ordinary least squares (OLS) linear regression was fitted for each month m:

$$SSM_{i,m} = a_m + b_m \phi_i + \varepsilon_{i,m} \tag{A7}$$

where a_m is the intercept and $\varepsilon_{i,m}$ is the residual term. The slope b_m (units: m^3/m^3 per degree latitude) was used as a monthly indicator of gradient strength; $b_m < 0$ indicates decreasing SSM with increasing latitude. The slope significance was determined jointly using the two-sided p-value $p_{b,m}$ and the 95% confidence interval (CI); the monthly gradient was considered significant when $p_{b,m} < 0.05$, or equivalently when $0 \notin CI_{95\%}(b_m)$.

Appendix A.3. Construction of Enhanced Precipitation Indices

This study constructs two antecedent precipitation metrics in addition to the baseline same-day precipitation variable: a fixed-window cumulative precipitation metric and an exponentially decayed antecedent precipitation index (API). Let t denote the SMAP overpass (acquisition) date and let $P(t)$ represent the CHIRPS daily precipitation aligned to date t.

All antecedent precipitation metrics are constructed with respect to the SMAP overpass date t and, by default, exclude same-day precipitation to avoid redundancy with the coincident precipitation information. To mitigate edge effects arising from insufficient antecedent records at the beginning of the study period (which could otherwise force antecedent metrics toward zero), we additionally collected daily precipitation data starting from 1 October 2023 as a spin-up period prior to the study window (December 2023–November 2024). This spin-up period was used solely to compute antecedent metrics such as $P_{14}(t)$ and $API_{\alpha,K}(t)$ and was not included in the model training/testing performance evaluation, ensuring that antecedent predictors for all samples in the study period were derived from consistent and sufficiently long precipitation histories.

(1) Cumulative precipitation. The fixed-window cumulative precipitation ending at date t is defined as the sum of daily precipitation over the preceding 14 days:

$$P_{14}(t) = \sum_{k=1}^{14} P(t-k) \tag{A8}$$

where $P(t-k)$ is the daily precipitation on day $t-k$. This metric represents the total precipitation input within a fixed look-back window.

(2) Antecedent precipitation index (API). To characterize the temporally decaying influence of antecedent rainfall on soil-moisture response, we define an exponentially decayed API as:

$$API_{\alpha,K}(t) = \sum_{k=1}^{K} \alpha^{k-1} P(t-k) \tag{A9}$$

where $\alpha \in (0,1)$ is the decay factor and K is the look-back window length. In this study, we set $\alpha = 0.90$ and $K = 60$ days to represent relatively long soil-moisture memory; this setting is denoted as API090 for brevity in the tables.

Appendix B.

Table A1. Seasonal and all-season base model performance comparison.

Model	Winter		Spring		Summer		Autumn		All Seasons	
	RMSE	**R^2**	**RMSE**	**R^2**	**RMSE**	**R^2**	**RMSE**	**R^2**	**RMSE**	**R^2**
ET	0.0157	0.9493	0.0283	0.8869	0.0341	0.8727	0.0256	0.8647	0.0299	0.8697
RF	0.0159	0.9479	0.0278	0.8909	0.037	0.8497	0.0280	0.8390	0.0317	0.8334
KNN	0.024	0.8810	0.0304	0.8689	0.0469	0.7592	0.0319	0.7904	0.0418	0.7443
XgBoost	0.0254	0.8664	0.0321	0.8540	0.0416	0.8102	0.0321	0.7875	0.0425	0.7367
CatBoost	0.0254	0.8664	0.0318	0.8568	0.0421	0.8060	0.0327	0.7796	0.0411	0.7535
LightGBM	0.0357	0.7371	0.0411	0.761	0.0505	0.721	0.0404	0.6639	0.0511	0.6129

The units of RMSE are m^3/m^3.

Table A2. Performance comparison of different models across seasons.

Model		Winter		Spring		Summer		Autumn	
		Train	**Test**	**Train**	**Test**	**Train**	**Test**	**Train**	**Test**
DNN	R^2	0.8625	0.8556	0.8558	0.8386	0.7508	0.7290	0.7289	0.7469
	RMSE	0.0258	0.0264	0.0319	0.0337	0.0477	0.0498	0.0362	0.0349
	MAE	0.0193	0.02	0.0246	0.026	0.0372	0.0388	0.0257	0.027
GBM	R^2	0.9284	0.9132	0.9144	0.8875	0.8715	0.8382	0.8625	0.8283
	RMSE	0.0186	0.0205	0.0246	0.0282	0.0343	0.0385	0.0258	0.0287
	MAE	0.0142	0.0157	0.019	0.0218	0.0263	0.0298	0.02	0.0224

Table A2. *Cont.*

Model		Winter		Spring		Summer		Autumn	
		Train	Test	Train	Test	Train	Test	Train	Test
DRF	R^2	0.9386	0.9123	0.906	0.8453	0.8829	0.815	0.8709	0.8029
	RMSE	0.0172	0.0206	0.0258	0.0330	0.0327	0.0412	0.0251	0.0308
	MAE	0.0131	0.0156	0.0198	0.0254	0.0254	0.032	0.0194	0.0238
SOBLE-Top5	R^2	0.9586	0.9632	0.9323	0.9389	0.8944	0.9078	0.8893	0.8977
	RMSE	0.0142	0.0133	0.0219	0.0208	0.0303	0.0291	0.0232	0.0222
	MAE	0.0104	0.0097	0.016	0.0151	0.0227	0.0217	0.017	0.0167

RMSE and MAE are expressed in units of m^3/m^3.

Table A3. Performance–efficiency trade-off results under different ensemble strategies and ensemble sizes (winter case study).

Top K	Blender		Stacking (Linear Regression)		Stacking (Optimal Basic Learner)	
	R^2	Train time (s)	R^2	Train time (s)	R^2	Train time (s)
Top 2	0.9127	940.16	0.9309	1330.97	0.9577	1495.49
Top 3	0.9173	976.42	0.9345	1339.29	0.9585	1487.64
Top 4	0.9078	987.12	0.9345	1464.96	0.9585	1501.50
Top 5	0.8966	1038.38	0.9345	1466.26	0.9586	1521.82

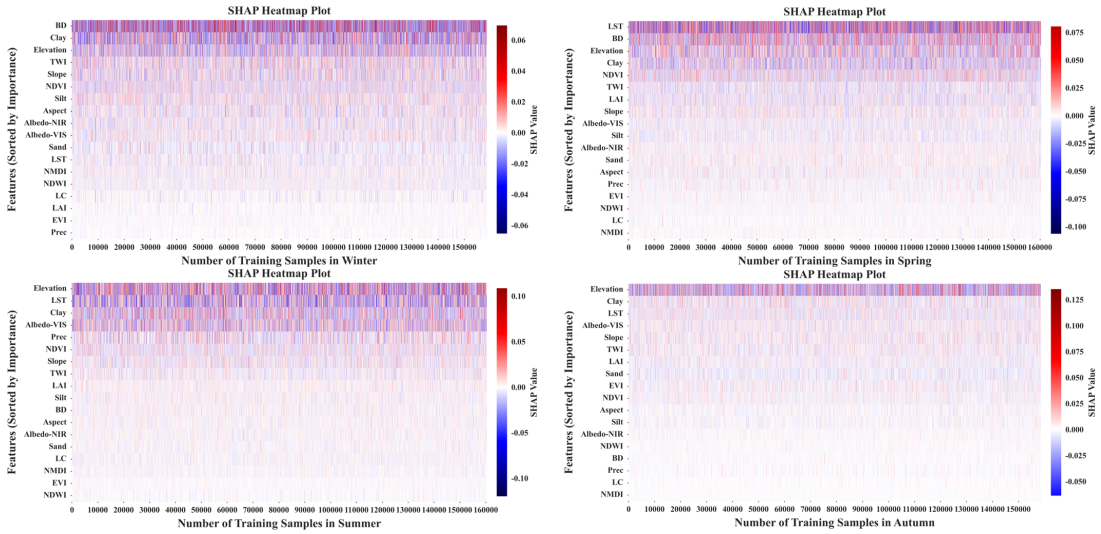


Figure A1. Heatmap visualization of SHAP values illustrating the contribution of each feature across all samples.

References

1. Ochsner, T.; Cosh, M.; Cuenca, R.; Dorigo, W.; Draper, C.; Hagimoto, Y.; Kerr, Y.; Larson, K.; Njoku, E.; Small, E.; et al. State of the Art in Large-Scale Soil Moisture Monitoring. *Soil Sci. Soc. Am. J.* **2013**, *77*, 1888–1919. [CrossRef]
2. Corradini, C. Soil moisture in the development of hydrological processes and its determination at different spatial scales. *J. Hydrol.* **2014**, *516*, 1–5. [CrossRef]
3. Wei, Y.; Lin, L.; Li, J.; Yuan, Q. A Soil Moisture Downscaling Residual Dense Network Considering Spatiotemporal Relationship. In *IGARSS 2023—2023 IEEE International Geoscience and Remote Sensing Symposium*; IEEE: New York, NY, USA, 2010; pp. 3170–3173.
4. Albergel, C.; de Rosnay, P.; Gruhier, C.; Muñoz-Sabater, J.; Hasenauer, S.; Isaksen, L.; Kerr, Y.; Wagner, W. Evaluation of remotely sensed and modelled soil moisture products using global ground-based in situ observations. *Remote Sens. Environ.* **2012**, *118*, 215–226. [CrossRef]
5. Njoku, E.G.; Entekhabi, D. Passive microwave remote sensing of soil moisture. *J. Hydrol.* **1996**, *184*, 101–129. [CrossRef]

6. Colliander, A.; Cosh, M.H.; Misra, S.; Jackson, T.J.; Crow, W.T.; Chan, S.; Bindlish, R.; Chae, C.; Holifield Collins, C.; Yueh, S.H. Validation and scaling of soil moisture in a semi-arid environment: SMAP validation experiment 2015 (SMAPVEX15). *Remote Sens. Environ.* **2017**, *196*, 101–112. [CrossRef]
7. Martínez-Fernández, J.; González-Zamora, A.; Sánchez, N.; Gumuzzio, A.; Herrero-Jiménez, C.M. Satellite soil moisture for agricultural drought monitoring: Assessment of the SMOS derived Soil Water Deficit Index. *Remote Sens. Environ.* **2016**, *177*, 277–286. [CrossRef]
8. Abowarda, A.S.; Bai, L.; Zhang, C.; Long, D.; Li, X.; Huang, Q.; Sun, Z. Generating surface soil moisture at 30 m spatial resolution using both data fusion and machine learning toward better water resources management at the field scale. *Remote Sens. Environ.* **2021**, *255*, 112301. [CrossRef]
9. Wagner, W.; Hahn, S.; Kidd, R.; Melzer, T.; Bartalis, Z.; Hasenauer, S.; Figa-Saldaña, J.; De Rosnay, P.; Jann, A.; Schneider, S. The ASCAT soil moisture product: A review of its specifications, validation results, and emerging applications. *Meteorol. Z.* **2013**, *22*, 5–33. [CrossRef]
10. Snoeij, P.; Attema, E.; Torres, R.; Levrini, G.; Croci, R.; L'Abbate, M.; Pietropaolo, A.; Rostan, F.; Huchler, M. C-SAR instrument design for the Sentinel-1 mission. In *2010 IEEE Radar Conference*; IEEE: New York, NY, USA, 2010; pp. 25–30.
11. Feng, X.; Li, J.; Cheng, W.; Fu, B.; Wang, Y.; Lü, Y.; Shao, M. Evaluation of AMSR-E retrieval by detecting soil moisture decrease following massive dryland re-vegetation in the Loess Plateau, China. *Remote Sens. Environ.* **2017**, *196*, 253–264. [CrossRef]
12. Cho, E.; Su, C.-H.; Ryu, D.; Kim, H.; Choi, M. Does AMSR2 produce better soil moisture retrievals than AMSR-E over Australia? *Remote Sens. Environ.* **2017**, *188*, 95–105. [CrossRef]
13. Wigneron, J.P.; Waldteufel, P.; Chanzy, A.; Calvet, J.C.; Kerr, Y. Two-Dimensional Microwave Interferometer Retrieval Capabilities over Land Surfaces (SMOS Mission). *Remote Sens. Environ.* **2000**, *73*, 270–282. [CrossRef]
14. Entekhabi, D.; Njoku, E.G.; Neill, P.E.O.; Kellogg, K.H.; Crow, W.T.; Edelstein, W.N.; Entin, J.K.; Goodman, S.D.; Jackson, T.J.; Johnson, J.; et al. The Soil Moisture Active Passive (SMAP) Mission. *Proc. IEEE* **2010**, *98*, 704–716. [CrossRef]
15. Parinussa, R.M.; Wang, G.; Holmes, H.T.R.; Liu, Y.Y.; Dolman, A.J.; de Jeu, R.A.M.; Jiang, T.; Zhang, P.; Shi, J. Global surface soil moisture from the Microwave Radiation Imager onboard the Fengyun-3B satellite. *Int. J. Remote Sens.* **2014**, *35*, 7007–7029. [CrossRef]
16. Jiang, X.; Mingsen, L.; Jianqiang, L.; Youguang, Z.; Xuetong, X.; Hailong, P.; Zhou, W. The HY-2 satellite and its preliminary assessment. *Int. J. Digit. Earth* **2012**, *5*, 266–281. [CrossRef]
17. Ebtehaj, A.; Bras, R.L. A physically constrained inversion for high-resolution passive microwave retrieval of soil moisture and vegetation water content in L-band. *Remote Sens. Environ.* **2019**, *233*, 111346. [CrossRef]
18. Chaubell, J.; Yueh, S.; Entekhabi, D.; Peng, J. Resolution enhancement of SMAP radiometer data using the Backus Gilbert optimum interpolation technique. In *2016 IEEE International Geoscience and Remote Sensing Symposium (IGARSS)*; IEEE: New York, NY, USA, 2016; pp. 284–287.
19. Gao, L.; Gao, Q.; Zhang, H.; Li, X.; Chaubell, M.J.; Ebtehaj, A.; Shen, L.; Wigneron, J.-P. A deep neural network based SMAP soil moisture product. *Remote Sens. Environ.* **2022**, *277*, 113059. [CrossRef]
20. Colliander, A.; Fisher, J.B.; Halverson, G.; Merlin, O.; Misra, S.; Bindlish, R.; Jackson, T.J.; Yueh, S. Spatial downscaling of SMAP soil moisture using MODIS land surface temperature and NDVI during SMAPVEX15. *IEEE Geosci. Remote Sens. Lett.* **2017**, *14*, 2107–2111. [CrossRef]
21. Peng, J.; Loew, A.; Merlin, O.; Verhoest, N.E.C. A review of spatial downscaling of satellite remotely sensed soil moisture. *Rev. Geophys.* **2017**, *55*, 341–366. [CrossRef]
22. El Hajj, M.; Baghdadi, N.; Zribi, M.; Belaud, G.; Cheviron, B.; Courault, D.; Charron, F. Soil moisture retrieval over irrigated grassland using X-band SAR data. *Remote Sens. Environ.* **2016**, *176*, 202–218. [CrossRef]
23. Sun, Y.; Liu, Q.; Wang, C.; Liu, Q.; Qu, Z. Improving Soil Moisture Estimation by Integrating Remote Sensing Data into HYDRUS-1D Using an Ensemble Kalman Filter Approach. *Agriculture* **2025**, *15*, 1320. [CrossRef]
24. Jiang, M.; Shen, H.; Li, J.; Zhang, L. Generalized spatio-temporal-spectral integrated fusion for soil moisture downscaling. *ISPRS J. Photogramm. Remote Sens.* **2024**, *218*, 70–86.
25. Xu, W.; Zhang, Z.; Long, Z.; Qin, Q. Downscaling SMAP Soil Moisture Products With Convolutional Neural Network. *IEEE J. Sel. Top. Appl. Earth Obs. Remote Sens.* **2021**, *14*, 4051–4062. [CrossRef]
26. Im, J.; Park, S.; Rhee, J.; Baik, J.; Choi, M. Downscaling of AMSR-E soil moisture with MODIS products using machine learning approaches. *Environ. Earth Sci.* **2016**, *75*, 1120. [CrossRef]
27. Wang, S.; Cai, Y.; Zhu, Z.; Xiudong, H.; Xiangwei, Z. Downscaling SMAP Soil Moisture Using a Combination of XGBoost and DSCGAN Algorithms. *J. Geo-Inf. Sci.* **2024**, *26*, 2213–2225. [CrossRef]
28. Poehls, J.; Alonso, L.; Koirala, S.; Reichstein, M.; Carvalhais, N. Downscaling soil moisture to sub-km resolutions with simple machine learning ensembles. *J. Hydrol.* **2025**, *652*, 132624. [CrossRef]
29. Koujani, S.R.; Hosseini, S.A.; Sharafati, A. Soil moisture downscaling in the state of Oklahoma: Employing advanced machine learning. *J. Atmos. Sol.-Terr. Phys.* **2025**, *268*, 106454.

30. Sabaghy, S.; Walker, J.P.; Renzullo, L.J.; Akbar, R.; Chan, S.; Chaubell, J.; Das, N.; Dunbar, R.S.; Entekhabi, D.; Gevaert, A.; et al. Comprehensive analysis of alternative downscaled soil moisture products. *Remote Sens. Environ.* **2020**, *239*, 111586. [CrossRef]
31. Wang, L.; Gao, Y. Estimating and Downscaling ESA-CCI Soil Moisture Using Multi-Source Remote Sensing Images and Stacking-Based Ensemble Learning Algorithms in the Shandian River Basin, China. *Remote Sens.* **2025**, *17*, 716. [CrossRef]
32. Senanayake, I.P.; Pathira Arachchilage, K.R.L.; Yeo, I.-Y.; Khaki, M.; Han, S.-C.; Dahlhaus, P.G. Spatial Downscaling of Satellite-Based Soil Moisture Products Using Machine Learning Techniques: A Review. *Remote Sens.* **2024**, *16*, 2067. [CrossRef]
33. Fang, B.; Lakshmi, V. Soil moisture at watershed scale: Remote sensing techniques. *J. Hydrol.* **2014**, *516*, 258–272. [CrossRef]
34. Xu, M.; Yang, H.; Hu, A.; Heng, L.; Li, L.; Yao, N.; Liu, G. A deep learning approach for SMAP soil moisture downscaling informed by thermal inertia theory. *Int. J. Appl. Earth Obs. Geoinf.* **2025**, *136*, 104370. [CrossRef]
35. Huete, A.; Didan, K.; Miura, T.; Rodriguez, E.P.; Gao, X.; Ferreira, L.G. Overview of the radiometric and biophysical performance of the MODIS vegetation indices. *Remote Sens. Environ.* **2002**, *83*, 195–213. [CrossRef]
36. Schaaf, C.B.; Gao, F.; Strahler, A.H.; Lucht, W.; Li, X.; Tsang, T.; Strugnell, N.C.; Zhang, X.; Jin, Y.; Muller, J.-P.; et al. First operational BRDF, albedo nadir reflectance products from MODIS. *Remote Sens. Environ.* **2002**, *83*, 135–148. [CrossRef]
37. Long, D.; Bai, L.; Yan, L.; Zhang, C.; Yang, W.; Lei, H.; Quan, J.; Meng, X.; Shi, C. Generation of spatially complete and daily continuous surface soil moisture of high spatial resolution. *Remote Sens. Environ.* **2019**, *233*, 111364. [CrossRef]
38. Wan, Z.; Zhang, Y.; Zhang, Q.; Li, Z.-l. Validation of the land-surface temperature products retrieved from Terra Moderate Resolution Imaging Spectroradiometer data. *Remote Sens. Environ.* **2002**, *83*, 163–180. [CrossRef]
39. Huang, S.; Zhang, X.; Wang, C.; Chen, N. Two-step fusion method for generating 1 km seamless multi-layer soil moisture with high accuracy in the Qinghai-Tibet plateau. *ISPRS J. Photogramm. Remote Sens.* **2023**, *197*, 346–363. [CrossRef]
40. Beven, K.J.; Kirkby, M.J. A physically based, variable contributing area model of basin hydrology/Un modèle à base physique de zone d'appel variable de l'hydrologie du bassin versant. *Hydrol. Sci. Bull.* **1979**, *24*, 43–69. [CrossRef]
41. Yang, N.; Xiang, F.; Zhang, H. The characterization of the vertical distribution of surface soil moisture using ISMN multilayer in situ data and their comparison with SMOS and SMAP soil moisture products. *Remote Sens.* **2023**, *15*, 3930. [CrossRef]
42. Li, G.; Hari, S.K.S.; Sullivan, M.; Tsai, T.; Pattabiraman, K.; Emer, J.; Keckler, S.W. Understanding error propagation in deep learning neural network (DNN) accelerators and applications. In *International Conference for High Performance Computing, Networking, Storage and Analysis*; ACM: New York, NY, USA, 2017; pp. 1–12.
43. Yang, K.; Painter, T.H.; Deems, J.S.; Molotch, N.P. Bias correction for near-real-time estimation of snow water equivalent using machine learning algorithms: A case study in the Tuolumne River basin, California. *Remote Sens. Environ.* **2025**, *323*, 114693. [CrossRef]
44. Vahidi, M.; Shafian, S.; Frame, W.H. Depth-specific soil moisture estimation in vegetated corn fields using a canopy-informed model: A fusion of RGB-thermal drone data and machine learning. *Agric. Water Manag.* **2025**, *307*, 109213. [CrossRef]
45. Babaeian, E.; Paheding, S.; Siddique, N.; Devabhaktuni, V.K.; Tuller, M. Estimation of root zone soil moisture from ground and remotely sensed soil information with multisensor data fusion and automated machine learning. *Remote Sens. Environ.* **2021**, *260*, 112434. [CrossRef]
46. Wolpert, D.H. Stacked generalization. *Neural Netw.* **1992**, *5*, 241–259. [CrossRef]
47. Zhang, X.; Jia, W.; He, J. Spatial and temporal variation of ecological quality in northeastern China and analysis of influencing factors. *J. Clean. Prod.* **2023**, *423*, 138650. [CrossRef]
48. Hu, L.; Zhou, Q.; Peng, D.; Shi, C.; Sun, Q.; Hu, Y.; Li, Y. Effects of vegetation restoration on the temporal variability of soil moisture in the humid karst region of southwest China. *J. Hydrol. Reg. Stud.* **2024**, *53*, 101852. [CrossRef]
49. Zhang, L.; Zhao, T.; Jiang, L.; Zhao, S. Estimate of phase transition water content in freeze–thaw process using microwave radiometer. *IEEE Trans. Geosci. Remote Sens.* **2010**, *48*, 4248–4255.
50. Ma, J.; Li, R.; Wu, T.; Liu, H.; Wu, X.; Hu, G.; Liu, W.; Wang, S.; Xiao, Y.; Tang, S.; et al. Dynamics of the Interaction between Freeze–Thaw Process and Surface Energy Budget on the Permafrost Region of the Qinghai-Tibet Plateau. *Land* **2024**, *13*, 1609. [CrossRef]
51. Lian, X.; Piao, S.; Li, L.Z.; Li, Y.; Huntingford, C.; Ciais, P.; Cescatti, A.; Janssens, I.A.; Peñuelas, J.; Buermann, W. Summer soil drying exacerbated by earlier spring greening of northern vegetation. *Sci. Adv.* **2020**, *6*, eaax0255. [CrossRef] [PubMed]
52. Lundberg, S.M.; Lee, S.-I. A unified approach to interpreting model predictions. *Adv. Neural Inf. Process. Syst.* **2017**, *30*.
53. Tang, H.; Sun, X.; Zhou, X.; Li, C.; Ma, L.; Liu, J.; Ding, Z.; Liu, S.; Yu, P.; Jia, L.; et al. Land Surface Temperature May Have a Greater Impact than Air Temperature on the Autumn Phenology in the Tibetan Plateau. *Forests* **2024**, *15*, 1476. [CrossRef]
54. Koehn, C.; Petrie, M.; Bradford, J.; Litvak, M.; Strachan, S. Seasonal Precipitation and Soil Moisture Relationships Across Forests and Woodlands in the Southwestern United States. *J. Geophys. Res. Biogeosci.* **2021**, *126*, e2020JG005986. [CrossRef]

Disclaimer/Publisher's Note: The statements, opinions and data contained in all publications are solely those of the individual author(s) and contributor(s) and not of MDPI and/or the editor(s). MDPI and/or the editor(s) disclaim responsibility for any injury to people or property resulting from any ideas, methods, instructions or products referred to in the content.